J. Fluid Mech. (1991), *vol.* 231, *pp.* 615–663
Printed in Great Britain

Longitudinal vorticity elements in boundary layers: nonlinear development from initial Görtler vortices as a prototype problem

By A. S. SABRY† AND J. T. C. LIU
The Division of Engineering, Brown University, Providence, RI 02912, USA

(Received 10 October 1990)

The nonlinear effects of longitudinal vorticity elements in boundary layers are studied via a prototype problem: the development of such vorticity elements from initial Görtler vortices in the amplified regime. While a time-dependent, quasi-two-dimensional formulation greatly simplifies the computational framework, full three-dimensionality of the velocity components is obtained. This temporal analogy for spatially developing flows approximates the nonlinear streamwise advection by a constant convection velocity, but the strong cross-sectional, advective nonlinearities are retained. Such an approximation lacks the stretching effect of the streamwise vorticity, since such elements are lifted into regions of higher streamwise velocities. That the temporal analogy is a good theoretical (and experimental) approximation to real developing flows is shown by *a posteriori* indications that the streamwise vorticity remains weak throughout the nonlinear region (though it has far-reaching nonlinear effects in upwelling in the peak region) and that the region of strong nonlinearities remains in the cross-sectional plane.

The aim of this work is to elucidate the nonlinearities producing sites of secondary instabilities and turbulence generation. The present mushroom-like computed iso-streamwise velocity contours surrounding the peak, as well as the streamwise velocity profiles in the peak and valley regions, agree well with experimental measurements up to the region of expected wavy secondary instabilities. Three local intense vorticity and enstrophy areas are found to be significant and these are thoroughly diagnosed. One such intense vorticity region arises from the upwelling of existing spanwise vorticity and subsequent spanwise stretching in the outer layers, leading to intense local high-shear layers of spanwise vorticity in the vicinity of the peak region, as expected. Primarily through the stretching of the vertical vorticity, intense vertical vorticity (and associated enstrophy) develop (i) in the shoulder regions of the mushroom-like iso-streamwise velocity structures in the outer layers of the boundary layer and (ii) in the inner regions of about thirty viscous lengths from the wall, close to the base of the mushroom-like structures. Of the three regions of intense local 'free' shear-layer vorticity, the vertical vorticity in the inner regions near the mushroom stem is dominant. This is entirely consistent with experimental observations of sites of high-frequency secondary and fine-scaled wavy instabilities. This theoretically/computationally obtained 'parent flow' essentially sets the stage for continued studies of its wavy instabilities. In order to analyse and control the shear stress at the wall and nonlinear flow development, the effect of initial parameters such as Görtler number, initial amplitudes and wavenumbers is fully explored.

† Present address: Department of Mechanical Engineering, Cairo University, Cairo, Egypt.

1. Introduction

Longitudinal vorticity elements and their nonlinear effects in boundary layers play a significant role in the later stages of transition (Stuart 1965), whether they are products of the nonlinear stages of Tollmien–Schlichting wave development or of initial Görtler vortices (Görtler 1940) arising from concave wall curvature. Initial experiments confirming instabilities and transition over concave surfaces were performed by Clauser & Clauser (1937) and Liepmann (1943, 1945). The importance of longitudinal vorticity elements in turbulent boundary layers is now well recognized (Kim, Kline & Reynolds 1971; Willmarth 1975). The fundamental importance of the role of longitudinal vorticity elements in the origin of turbulence in wall-bounded shear flows was recognized by Prandtl (1935) quite some time ago. Conceptually, Prandtl imagined the existence of weak, longitudinal vortex motions in the form of spanwise-periodic, counter-rotating vorticity elements aligned in the streamwise direction. Imagining a cross-sectional cut normal to the streamwise direction would show that the effect of these elements is to give rise to advecting velocities that cause the boundary layer to shift sideways at alternate nodes and to deposit part of the low-momentum fluid into the upper unretarded flow regions. This creates regions of inflexional velocity profiles that are unstable and could break down into secondary motions. Prandtl further remarks, 'In practice it is observed that vortices produced by the disintegration of an unstable flow multiply, as a rule, very quickly, so that once such vortices are present, turbulence soon spreads throughout the whole flow.' Prandtl (1935) then concludes that, while turbulence could be generated by such a phenomenon, 'no theoretical explanation has hitherto been possible.'

Prandtl's remarkable insight was confirmed in the 1960s by detailed experiments on boundary-layer transition (Klebanoff, Tidstrom & Sargent 1962; Kovasznay, Komoda & Vasudera 1962; Hama & Nutaant 1963). These experiments are discussed by Stuart (1965) in terms of nonlinear development of small disturbances arising from plane Tollmien–Schlichting waves upstream. The modulated, longitudinal vorticity elements arising from Tollmien–Schlichting waves, however, are much more intricate and we refer the reader to recent reviews of this subject (Stuart 1986; Herbert 1987).

Stuart (1965), however, shows that the generation of three-dimensional high-shear layers within the boundary layer can completely bypass the Tollmien–Schlichting mechanism. He constructed a kinematic model, in the absence of streamwise modulation, to elucidate the effect of vorticity advection and stretching in the formation of inflexional streamwise velocity profiles in the upper layers of the boundary layer. Stuart assumed a time-developing but streamwise-independent flow and specified the spanwise periodic longitudinal vorticity elements pertaining to the cross-sectional flow. As such, the longitudinal vorticity elements remain passive in that they do not exchange energy with the mean motion. The unknown streamwise velocity would then be given by a linear equation. The generation of intense high-inflexional shear layers at the 'peaks' was brought out by the characteristic solution to the inviscid problem. In the peak region it is first the vertical velocity associated with longitudinal vorticity element that advects upwards the low-momentum fluid and high spanwise vorticity associated with the basic flow, and second the spanwise stretching of this advected vorticity by the spanwise velocity associated with the upper region of the longitudinal vorticity elements. Stuart (1965) depicts this interaction between longitudinal vorticity elements and the basic boundary-layer shear in terms of a spanwise perturbation of vorticity elements originally lying in the spanwise direction. After a spanwise-periodic perturbation, the vorticity develops

into uplifted horseshoe-like vorticity elements at the peak regions. Though a kinematic calculation, Stuart (1965) obtained a timescale for high-shear-layer development that resembled that found in experiments (Klebanoff *et al.* 1962). More recently, Stuart's (1965) framework has been extended to a finite-span 'flat eddy' by Russell & Landahl (1984) and has also been used by Pearson & Abernathy (1984), Moore (1985) and Yang (1987) in connection with a single longitudinal vortex and the effect of viscosity. The nonlinear features of such problems are discussed by Stuart (1987) in the inviscid case where all three components of the flow velocity are coupled. The full three-dimensionality of the 'basic' flow is, as we shall see, an important feature of transition and turbulence generation.

The longitudinal vorticity elements and their consequences play a significant role well beyond the wall-bounded shear-flow transition problem as originally envisioned by Prandtl (1935). They have been found to be omnipresent in turbulent boundary layers (Kline *et al.* 1967; Corino & Brodkey 1969; Kim *et al.* 1971; Willmarth 1975; Blackwelder & Kaplan 1976). The formation of high-shear layers there, in fact, is part of the cyclic burst-and-sweep process intimately associated with the bursting events and fine-grained turbulence generation (Willmarth 1975; Kim *et al.* 1971; Blackwelder & Kaplan 1976). More recently, the importance of the vorticity normal to the wall associated with nonlinearly modified spanwise periodicity in causing secondary instabilities in transition has been emphasized by Swearingen & Blackwelder (1987); this is discussed fully in §7 below.

The strong analogy between the effects of longitudinal vorticity elements in transitional and turbulent boundary layers has been pointed out by Blackwelder (1983). The analogy is brought out by a scaling using wall variables, i.e. scaling lengths and velocities by ν/u_τ and u_τ respectively, where ν is the kinematic viscosity and u_τ the mean friction velocity. Recently, Swearingen & Blackwelder (1987) compared their time-averaged streamwise velocity profile along a single 'peak' region that developed from upstream Görtler vortices, and showed the strong similarity between their 'intermediate' stage of inflexion velocity profile development, a local flat-plate, transitional profile (Kovasnay *et al.* 1962) and a local profile associated with the ejection event of the turbulent boundary layer (Grass 1971). The mean turbulent boundary-layer profile was also shown to be similar to the streamwise velocity along the peak region at the mature stages of transition (Swearingen & Blackwelder 1987) due to upstream Görtler vortices. Although such analogies are most certainly local in nature, they show the role of longitudinal vorticity elements in boundary layers to be much more universal than originally envisioned by Prandtl (1935), though his mechanisms continue to prevail. From a theoretical point of view, it would be helpful to study their role by using the dynamical equations from an extension of the kinematic considerations of Stuart (1965). The understanding gained from the dynamics could possibly lead to the control of the formulation of internal free-shear layers and of the consequential generation of turbulence in transitional and turbulent boundary layers. In this case, the nonlinear development of longitudinal vorticity elements from upstream Görtler vortices is both an appropriate (Blackwelder 1983) and convenient prototype problem to study. Longitudinal vorticity elements can always be generated mechanically (e.g. Yurchenko 1981) or via an initial concave region, prior to studying their effect on transition in boundary layers (Tani & Komoda 1962). The technological importance of such studies is amply demonstrated by transition problems on turbine and compressor blades (Shigemi, Johnson & Gibbings 1987; Peerhossaini 1984) and on airfoils (Mangalam *et al.* 1985; Dagenhart & Mangalam 1986).

Finally, no attempt is made here to review comprehensively all the literature on longitudinal vorticity elements and Görtler vortices. We refer to the review by Peerhossaini (1985) as well as reviews by Hall (1989) and by Saric (1992).

2. Discussion of the problem

Our aim is to address the nonlinear development of longitudinal vorticity elements in the boundary layer and the consequential formation of local intense free-shear layers,† with emphasis on comparisons with and interpretation of recent quantitative experimental measurements (e.g. Ito 1980, 1985; Aihara & Koyama 1982*a*, *b*; Aihara, Tomito & Ito 1985; Swearingen & Blackwelder 1987). Experimentally, the primary disturbance has a streamwise developing structure that is independent of time, whereas the secondary instabilities are modulated in time and in the streamwise distance (Swearingen & Blackwelder 1987). In this paper we concentrate on the nonlinear development of the primary structure.

To this end, longitudinal vorticity elements developing from initial Görtler vortices are the subject of our study. Görtler vortices are themselves longitudinal, but they require sufficient concave-wall curvature to overcome the viscous retardation of their incipient existence. Experimentally, such vortices almost always correspond to the amplified regime (Tani & Aihara 1969; Tani 1962; Bippes 1972; Peerhossaini 1984, 1985; Babenko & Yurchenko 1980; Winoto & Crane 1980; Yurchenko, Babenko & Kozlov 1979; Wortmann 1969), according to the linear theory (e.g. Herbert 1976; Smith 1955; Floryan & Saric 1982), and once established, they persist even on flat walls (Peerhossaini & Wesfreid 1987). Theoretically, for amplified disturbances, the Reynolds shear-stress conversion mechanism plays the dominant role in amplifying and strengthening the developing disturbance downstream; the concave-curvature effect, on the other hand, except for its incipient role, has almost a secondary effect downstream.

Herbert (1976), Floryan & Saric (1982) and Hall (1983) have reviewed the linearized theory of Görtler vortices. Unlike the situation in which Taylor vortices are confined between rotating cylinders, where the linear theory enjoyed experimental verification from the outset (Taylor 1923), controversies and inconsistencies beset the linear parallel-flow theory for Görtler vortices. It appears that 'accurate' calculations of the neutral curve, based on Görtler (1940) theory, place the minimum Görtler number at essentially zero dimensionless spanwise wavenumber (Hammerlin 1955; Herbert 1976; Floryan & Saric 1982). There are large discrepancies between the linear theories, which are based on ordinary differential equations that neglect the streamwise evolution history and that for the developing boundary layer (Hall 1983).

The existence of a neutural curve in real, developing boundary layers is, in fact, open to question. Hall (1983) shows that, with appropriate scaling, even the linear problem is an initial-value problem governed by parabolized partial differential equations. The streamwise distance plays the role of 'time'. The neutral condition would be obtained at a particular streamwise location where the total kinetic energy of the disturbance reaches a maximum. As an initial-value problem, the solution (and hence the growth rate) is naturally sensitive to the initial parameters and energy levels and possibly even the location where the initial condition is applied. The neutral curve from the initial-value problem attains a minimum Görtler number at a finite wavenumber (Hall 1983). However, in the context of developing boundary

† We are aware of similar work by W. Liu & J. A. Domaradzki and C.-W. Park & P. Huerre which, hopefully will be available in the archival literature soon.

layers, the search for the neutral curve is no longer meaningful, as it would be for parallel flow (Hall 1983). The 'neutral condition', which is where the disturbance energy reaches a maximum, occurs at only one station (or stations) along the streamwise distance. In fact, the overall streamwise evolution of the energy as well as of the local states is central to the initial-value problem. This characterization is apparently lost in the parallel-flow problem.

The Görtler number–wavenumber plane is nevertheless an important guide for experimental measurements that involve developing boundary layers (Floryan & Saric 1982; Hall 1983; Swearingen & Blackwelder 1987). In terms of the local momentum thickness θ, the Görtler number is defined as $G_\theta = U_0\theta/\nu(\theta/R)^{\frac{1}{2}}$, where U_0 is the free-stream velocity, ν the kinematic viscosity and R the radius of concave wall curvature (essentially the Taylor number, Taylor 1923); this can be recast into the form $G_\theta = \Lambda_\alpha(\theta\alpha)^{\frac{3}{2}}$, where α is the spanwise wavenumber and $\Lambda_\alpha = Re_R(\alpha R)^{-\frac{3}{2}}$, where $Re_R = U_0R/\nu$ is the curvature Reynolds number. It is clear that, for a robust, constant wavenumber observed in an experiment, the local Görtler number increases as $\theta^{\frac{3}{2}}$ for a given experiment, with the coefficient Λ_α a constant characterizing particular experiments in the $(G_\theta, (\alpha\theta))$-plane (Swearingen & Blackwelder 1987). However, Swearingen & Blackwelder define the coefficient Λ using the wavelength $\lambda = 2\pi/\alpha$, so that $\Lambda_\lambda = Re_R(\lambda/R)^{\frac{3}{2}}$. Although statistically their experiments gave $\lambda \approx 2.30$ cm (corresponding to $\Lambda_\lambda \approx 650$), the actual quantitative data to which we compare our results were for $\lambda \approx 1.80$ cm, for which $\Lambda_\lambda \approx 460$. This choice is because the detailed measurements were made within the $\lambda = 1.80$ cm longitudinal vorticity elements; in addition, computed results for $\lambda \approx 2.30$ cm gave poor comparisons with $\lambda \approx 1.80$ cm measurements. The experiments of Tani (1962) lie in the range $\Lambda_\lambda \approx 650$–$1890$; in those of Bippes (1972), $\Lambda_\lambda \approx 210$; in those of Aihara & Koyama (1982*a*, *b*), $\Lambda_\lambda \approx 235$, and in that of Ito (1985), $\Lambda_\lambda \approx 345$. The observed incipient Görtler instabilities occur without exception in the 'amplified region' and follow a Λ_α or Λ_λ = constant line in their nonlinear development. For the unsteady boundary layer on the interior wall of a suddenly stopped rotating cylinder, Kozlov, Glushko & Nikishova (1981) obtained $\Lambda_\lambda \approx 440$.

Hall (1982*a*, *b*), Hall & Lakin (1988*a*, *b*) and Hall & Seddougui (1980) study various aspects of Görtler vortices in developing boundary layers by employing asymptotic analysis with the spanwise wavelength relative to the boundary-layer thickness taken as a small parameter. In developing the linear theory, Hall (1982*a*) concentrated on the upper right-hand branch of the neutral curve and showed that in this limit a unique neutral curve is obtained according to linear parallel-flow theory; systematic corrections due to boundary-layer growth can be applied. Boundary-layer growth indeed becomes unimportant when the wavelengths are small. The corresponding weakly nonlinear theory in the neighbourhood of the neutral curve was also obtained by Hall (1982*b*). The significant result is that the nonlinearity resembles the mean field interaction of Meksyn & Stuart (1951) in that a dominant fundamental interacts with the mean flow and harmonic generation is secondary. The Görtler structure obtained is in the outer part of the boundary layer.

In order to maintain a neutral solution in the linear problem, it was necessary that the Görtler number increases as the square root of the downstream distance (Hall 1982*a*), but that could be interpreted as maintaining a definite variable wall curvature downstream (Hall 1982*b*). Apparently, in the small-wavelength regime near the neutral curve, the rate of downstream increase of curvature must be large enough for the disturbance to overcome the viscous retardation effects. The weak nonlinearity restricts the solution to the vicinity of the neutrally stable disturbance, where the mechanism of Reynolds stress energy conversion from the mean flow

would be unimportant, in contrast to amplified disturbances in an experimental situation.

In the small-wavelength limit, the weak nonlinearity restrictions are removed and extended to full nonlinear conditions (Hall & Lakin 1988*a*, *b*). The mean field interaction is recovered. Again the Görtler structure is in the outer part of the boundary layer and a downstream increase in curvature accompanies the solution. Inflexional mean profiles normal to the wall did not develop downstream. Hall & Lakin's development of the full nonlinear solution forms the basis of linear studies of secondary instabilities in the form of three-dimensional wave disturbances (Hall & Seddougui 1989) in the spirit of the study by Davey, DiPrima & Stuart (1968) of instability of Taylor vortices.

Some aspects of the analyses using small dimensionless wavelengths are helpful in understanding some of the main aspects of the longitudinal vorticity elements developing from highly amplified Görtler vortices at finite wavenumbers. However, in the main they are irrelevant to the real, observed experimental situations. Hall (1988) also addressed this problem by numerically integrating parabolized partial differential equations after making the Fourier expansion with truncation in the spanwise modes. Although inflexional mean velocities were obtained, the numerical integration was carried out with variable wall curvature, and quantitative comparisons with experiments for constant wall curvature were absent. In a later work, Hall (1989) compared his numerical results with the experimental results of Swearingen & Blackwelder (1987) but obtained only qualitative agreement. Perhaps the reasons for lack of quantitative comparison are first the implicit weak nonlinear assumptions in the cross-sectional plane and secondly that his initial conditions were not hydrodynamically possible ones. We address the initial-condition issue in §3. Hall's expansion of flow quantities in the spanwise nZ harmonics (where Z is the spanwise distance) resulted in amplitudes in X, Y (where X is the streamwise distance and Y normal to the wall), retaining terms up to $n = 4$. Detailed measurements show (Swearingen & Blackwelder 1987) that while the nonlinear development is periodic in Z, it is not representable by the first few sines and cosines in Z. Apparently, the nonlinearities are much stronger in the (Y, Z)-plane than the weakly nonlinear truncation in Z could describe. The partial differential equation solution in the (X, Y)-plane emphasizes the inessential nonlinearities in X. The present work, obtained without harmonic expansions in Z, shows from the finite-difference solution that strong nonlinearities in the (Y, Z)-plane indeed contribute to the strong nonlinear distortions of the flow and capture the flow pattern observed in experiments. The present work is thus intended to emphasize and bring out the essential nonlinearities in the (Y, Z)-plane while approximating the inessential nonlinearities in X by the simple time evolution. In fact, the strong nonlinearities in the (Y, Z)-plane are pivotal in the development of a theory that is sufficiently realistic to be reconciled with quantitative details of experimental measurements. This is the primary goal of the present work.

3. Formulation and basic equations

We formulate the nonlinear development of longitudinal vorticity elements in terms of temporal rather than spatial development. The nonlinear streamwise advection is mimicked by time development, and streamwise derivatives of all flow quantities are absent (Stuart 1965). For incompressible flow, the absence of streamwise derivatives renders the continuity equation two-dimensional and a cross-section-plane stream function can thus be introduced. The latter, in turn, can be

related to the streamwise component of the vorticity. This makes possible the simplification of describing the nonlinear evolution in terms of only two, coupled nonlinear parabolic partial differential equations for the streamwise velocity and vorticity, instead of the original four. The parabolicity follows from the absence of streamwise derivatives in conjunction with time development. In the spatial problem, parabolicity would follow from a large-Reynolds-number approximation (Hall 1983).

As in Stuart (1965), we need not perform the Reynolds splitting at the outset. Subsequent spanwise averaging is equivalent to such a splitting procedure, since the only periodicity is in the spanwise direction. In the absence of disturbances, the temporal mean flow problem is simply the Rayleigh–Stokes problem governed by the linear heat diffusion equation, whereas the spatial problem corresponds to the nonlinear Blasius problem for large Reynolds number. Although the one-to-one correspondence is absent, the temporal problem retains many of the physical features and hence contributes to the understanding of the spatial problem with considerable simplification. The temporal problem here corresponds to an 'Oseen approximation' applied to the nonlinear streamwise-advective derivatives. That this would be found to be a reasonable approximation was suggested by both experimental (Swearingen & Blackwelder 1987) and computational (Sabry & Liu 1988*a*) indications that strong nonlinearities in the cross-sectional plane prevail over those in the streamwise direction In this situation, streamwise advection is essentially accomplished by a constant velocity. The strong nonlinearities in the cross-sectional plane exist in conjunction with weak streamwise vorticity and gradients in real flows.

The temporal problem is that of a fluid in solid-body rotation contained in a rotating cylinder. The viscous boundary layer develops after the cylinder is suddenly stopped, while the interior fluid is still in motion. The analogy with the spatial boundary layer holds as long as the viscous development length $\delta \sim (\nu/T)^{\frac{1}{2}}$ (where T is time) is small compared to the radius of the cylinder. In this case, $\delta/R \ll 1$ and curvature effects on the viscous boundary layer itself are not important. The temporal problem is axially symmetric, with no circumferential derivatives of flow quantities. The experimental possibility of the temporal development of Görtler vortices is discussed by Kozlov *et al.* (1981) and much earlier by Frażer (1931) who also obtained a linear theory accounting for the growth of the time-developing basic flow.

The equations of motion and of continuity for cylindrical coordinates may be found, for instance, in Batchelor (1967). These can be translated (Görtler 1940) to the corresponding orthogonal coordinate system place on the stationary wall, with X, Y, Z the coordinates in the circumferential (streamwise, along the curved wall), normal and axial (spanwise) directions, respectively. We denote the respective velocities as U, V and W; P is the pressure.

We denote a typical timescale by $T_0 = X_0/U_0$, where X_0 would be a typical lengthscale in the spatial problem; U_0 is the 'free-stream velocity' and is identical to the circumferential velocity of the cylinder prior to its stoppage. In the thin viscous-layer approximation, normal and spanwise lengthscales would be then described by the viscous length $\delta_0 = (\nu T_0)^{\frac{1}{2}}$. We rescale the equations of motion through the following dimensionless quantities (denoted by lower-case symbols):

$$t = \frac{T}{T_0}, \quad y = \frac{Y}{\delta_0}, \quad z = \frac{Z}{\delta_0}, \quad u = \frac{U}{U_0}, \quad v = \frac{V}{U_0} Re^{\frac{1}{2}}, \quad w = \frac{W}{U_0} Re^{\frac{1}{2}}, \quad p = \frac{P}{\rho U_0^2} Re, \tag{3.1}$$

where ρ is the density. The appropriate Reynolds number Re here is

$$Re = U_0(U_0 T_0)/\nu. \tag{3.2}$$

In the above scaling, which is similar to that introduced by Hall (1983), V and W are essentially scaled by the velocity scale $\rho(\delta_0/T_0)^2$. We emphasize again that the 'axial symmetry' implies that derivatives with respect to $x = X(U_0/T_0)$ do not appear.

To order (δ_0/R), the dimensionless continuity and momentum equations for the temporal problem have the form

$$\frac{\partial v}{\partial y}+\frac{\partial w}{\partial z} = 0, \tag{3.3}$$

$$\frac{\partial u}{\partial t}+v\frac{\partial u}{\partial y}+w\frac{\partial u}{\partial z} = \nabla_c^2 u, \tag{3.4}$$

$$\frac{\partial v}{\partial t}+v\frac{\partial v}{\partial y}+w\frac{\partial v}{\partial z}+G^2u^2 = -\frac{\partial p}{\partial y}+\nabla_c^2 v, \tag{3.5}$$

$$\frac{\partial w}{\partial t}+v\frac{\partial w}{\partial y}+w\frac{\partial w}{\partial z} = -\frac{\partial p}{\partial z}+\nabla_c^2 w, \tag{3.6}$$

where $G = (U_0\delta_0/\nu)(\delta_0/R)^{\frac{1}{2}}$ is the appropriate Görtler number, and ∇_c^2 is the Laplacian in the cross-sectional plane,

$$\nabla_c^2 = \frac{\partial^2}{\partial y^2}+\frac{\partial^2}{\partial z^2}. \tag{3.7}$$

Although in dimensional form, Görtler's (1940) original nonlinear equations, which form the starting point of his linear parallel-flow (i.e. boundary-layer growth frozen in time) studies, are equivalent to (3.3)–(3.6). In the temporal problem, the boundary layer grows in time and the growth is uniform circumferentially (or parallel in the streamwise direction). The longitudinal vorticity elements would develop within such a time-growing boundary layer.

We make another observation before proceeding further. The Görtler curvature effect, G^2u^2, in (3.5) appears as U^2/R in dimensional form. Its contribution to the total kinetic energy balance is then VU^2/R, and it is thus an 'energy source'. This is due to the neglect of $-UV/R$ (Hammerlin's 1955 mechanism) in the x-momentum equation in the scale analysis, which would contribute to $-U^2V/R$ and effect a cancellation of VU^2/R from the y-momentum contribution to the energy. We will see that when we consider numerical examples, the Reynolds shear-stress conversion mechanism for amplified disturbances is supplemented by the Görtler mechanism. The latter is required to set up the initial longitudinal vorticity system at finite Görtler numbers and wavenumbers.

The two-dimensional form of the continuity equation (3.3) in the cross-sectional (y, z)-plane suggests the stream function ψ:

$$v = -\frac{\partial\psi}{\partial z}, \quad w = \frac{\partial\psi}{\partial y}. \tag{3.8}$$

A single equation for the streamwise vorticity ξ is obtained from (3.5) and (3.6) through the definition

$$\xi = \frac{\partial w}{\partial y}-\frac{\partial v}{\partial z}. \tag{3.9a}$$

In the temporal system, the remaining vertical and spanwise vorticity components are, respectively

$$\eta = \frac{\partial u}{\partial z}, \quad \zeta = -\frac{\partial u}{\partial y}; \tag{3.9b, c}$$

η and ζ can be obtained once u has been computed. In the velocity–vorticity system of dependent variables, the system (3.3)–(3.6) reduces to (in conservation form)

$$\frac{\partial u}{\partial t} + \frac{\partial}{\partial y}\left[-\frac{\partial \psi}{\partial z}u\right] + \frac{\partial}{\partial z}\left[\frac{\partial \psi}{\partial y}u\right] = \nabla_c^2 u, \tag{3.10}$$

$$\frac{\partial \xi}{\partial t} + \frac{\partial}{\partial y}\left[-\frac{\partial \psi}{\partial z}\xi\right] + \frac{\partial}{\partial z}\left[\frac{\partial \psi}{\partial y}\xi\right] - G^2\frac{\partial u^2}{\partial z} = \nabla_c^2 \xi, \tag{3.11}$$

with

$$\xi = -\nabla_c^2 \psi. \tag{3.12}$$

We note that (3.11), (3.12) form the usual fourth-order equation for the stream function

$$\frac{\partial}{\partial t}\nabla_c^2 \psi + \frac{\partial}{\partial z}\left[-\frac{\partial \psi}{\partial z}\nabla_c^2 \psi\right] + \frac{\partial}{\partial z}\left[\frac{\partial \psi}{\partial y}\nabla_c^2 \psi\right] + G^2\frac{\partial u^2}{\partial z} = \nabla_c^4 \psi, \tag{3.13}$$

which, together with (3.10), constitute the reduction to two equations for u and ψ. Unlike the formulation arising from Stuart (1965), (3.10) and (3.13) are coupled through the Görtler curvature effect. For numerical computations, the system of three equations (3.10)–(3.12) is preferred. In either case, the stream function–vorticity formulation has the advantage of circumventing the explicit presence of the pressure in the dynamical equations.

The following boundary conditions are stated for the framework (3.10)–(3.12). The wall boundary conditions follow from the no-slip conditions for the velocities

$$y = 0: \quad u = 0, \quad \psi = 0, \quad \xi = \frac{\partial^2 \psi}{\partial y^2}. \tag{3.14}$$

Far from the wall, disturbances vanish, so that

$$y \to \infty: \quad u = 1, \quad \psi = 0, \quad \xi = 0. \tag{3.15}$$

For a single spanwise mode of dimensionless wavenumber α, it is sufficient to specify symmetry conditions at the half-wavelength π/α, so that

$$z = 0, \pi/\alpha: \quad \partial u/\partial z = 0, \quad \psi = 0, \quad \xi = 0. \tag{3.16}$$

The half-wavelength symmetry condition (3.15) has the advantage of reducing, at least by half, the computational effort needed relative to the full-wavelength periodic boundary conditions.

The initial conditions for the temporal problem are meant to simulate the local upstream occurrence of Görtler vortices in the experimentally observed spatial problem. In this case, the initial time for imposition of the disturbance is $T_i/T_0 = U_0/U_c$ for the temporal problem, where U_c is an advection velocity corresponding to the upstream condition at X_0 in the spatial problem (i.e. $T_i = X_0/U_c$); the corresponding development variables are related as $(T/T_0) = (X/X_0)(U_0/U_c)$. The shape of the initial disturbance corresponds to that obtained from the linearized version of (3.3)–(3.6), originally obtained by Görtler (1940) at the prevailing mean flow and Görtler number at X_0. The initial amplitude of the Görtler streamwise velocity is obtained by equating its maximum spanwise root-mean-square value to the experimentally measured value. It first appears that, in order to compare with

spatial experiments, two free parameters exist, X_0 and U_c. It is expected from elementary considerations that, even without disturbances, the mean flow in the present problem satisfies the heat equation approximately, whereas the spatial problem satisfies the Blasius boundary-layer equation. If the calculations were started too early, the mean flow would dominate and the linearized amplification rates due to a mean flow of the heat-equation type and of the Blasius type would be quite different. In this sense the calculations must necessarily start in a region where the disturbances are strongly amplified and attain dominance in order to dwarf the difference in the mean flow effect. Only in this sense is X_0 no longer a free parameter (provided that the initial disturbance imposed is a *hydrodynamically possible* one at the same consistent A_λ), but U_c remains as a free parameter. Hall's initial conditions (1983, 1988, 1989), though satisfying continuity, contain no information on A_λ, and hence X_0 becomes a free parameter.

In the present problem, the initial shape of the disturbance is generated according to linear theory. We followed known numerical procedures (e.g. Floryan & Saric 1982) that use the code (Support) developed by Scott & Watts (1977) for boundary-value problems in ordinary differential equations.

The present Görtler vortex problem is a semi-infinite problem corresponding to an open flow with $\delta/R \ll 1$. Curvature effects, except for the Görtler centrifugal mechanism, are appropriately neglected. The present unsteady boundary-layer formulation (3.10), (3.11) is reminiscent of the Taylor–Couette closed-flow problem considered by Liu & Chen (1973). Their algorithm was used by Nikishowa (Kozlov *et al.* 1985)† in numerical experiments (starting with initial random numbers at different amplitudes) on the Görtler vortex problem, with qualitative comparisons to Aihara & Koyama's (1981) flow visualization observations.

4. Computational procedures

We solve equations (3.10)–(3.12) subject to the above initial and boundary conditions via finite-difference schemes. They are written in 'conservation' form in order to give, after discretization, a better numerical representation of the net flux through the finite-difference element than the non-consecutive form (Thompson, Warsi & Mastin 1985). In the present form (3.10) and (3.11) are two-dimensional parabolic and (3.12) two-dimensional elliptic.

Because the total flow variables used here develop close to the wall and vanish away from the wall, a transformation of the normal coordinate y into η is necessary to accommodate a denser mesh in the wall region:

$$\eta = (y-\beta)/(y+\beta), \tag{4.1}$$

where $y = 0, \infty$ corresponds to $\eta = \pm 1$ and β is a parameter to be specified that depends on the desired numerical mesh density near the $y \approx 0$ or $\eta \approx 1$ boundary. In this case, all y-derivatives in the problem are replaced by

$$\frac{\partial}{\partial y} = \frac{(1-\eta)^2}{2\beta}\frac{\partial}{\partial \eta}, \tag{4.2}$$

with the form of the equations remaining the same as (3.10)–(3.12).

In solving the system of equations (3.10)–(3.12) we followed a procedure similar to that suggested by Pearson (1965) and Aziz & Hellun (1967). We first guess the value

† I am indebted to Dr O. D. Nikishowa for this observation (private communication, Kiev 1989).

of the stream function at the next time step via linear interpolation. Then we obtain the corresponding values of the streamwise velocity and the streamwise vorticity by solving equations (3.10) and (3.11) respectively, using the alternating direction implicit (API) method introduced by Peaceman & Rachford (1955). In general, implicit schemes are to be preferred because of their stability properties. However, we use the successive over-relaxation (SOR) method in solving equation (3.12) to obtain a better estimate for the value of the stream function, since SOR is an efficient method if an initial guess close to the solution is known. Finally, an iteration procedure is performed until the initial guess for the stream function agrees with the solution of equation (3.12).

To check the numerical scheme, three tests are carried our:

(i) compare the behaviour of the solution as either Δt, Δz, or $\Delta\eta$ decreases for fixed values of time and normal and spanwise integration domain;

(ii) compare the behaviour of the solution with the case in which a decomposition of the streamwise velocity is used, so that $u = \bar{u}(y,t)+u'(y,z,t)$, where $\bar{u}$ is the spanwise-averaged mean flow and u' the disturbance;

(iii) compare the integration of the linear problem with the expected linear growth.

The above tests were successful and ensured the accuracy of the numerical scheme. It is also important to mention that, even though the ADI method is unconditionally stable in time, a large time step would cause the number of iterations to increase and the accuracy to decrease. Therefore in order to obtain high accuracy as well as to minimize the number of iterations, we restricted our time step to not exceed that required by the stability condition of the explicit scheme for linear parabolic equations (i.e. the von Neumann condition):

$$\Delta t(\Delta z^{-2}+\Delta y_{\min}^{-2}) \leqslant \tfrac{1}{2}.$$

The choice of a numerical mesh adequate to reveal accurately the details of the flow structure is an important step in the numerical procedure. We selected our mesh by choosing:

(i) the total number of grid points in the spanwise direction (17) equal to the number of the different y-rake locations used in the experiment (Swearingen & Blackwelder 1987) to cover half the spanwise wavelength;

(ii) the total number of grid points in the normal direction (201) to cover a length of $50\delta_0$;

(iii) the parameter $\beta = 50$ in the coordinate transformation $\eta = (y-\beta)/(y+\beta)$.

Such a choice has the advantage that both the normal and spanwise sizes of the mesh (Δy and Δz) are of comparable magnitudes. As already mentioned, to obtain high time accuracy as well as to minimize the number of iterations, we specifically restricted our time step to be $\Delta t = 6.831\times10^{-3}$, as small as the time step required by the von Neumann stability condition.

In the SOR method, we found that a relaxation factor of 1.83 allowed fast convergence.

5. Quantitative comparisons with experiments

In §§1 and 2, we have placed the nonlinear development of longitudinal vorticity elements within the much broader perspective of transitional and fully turbulent boundary layers, focusing on the omnipresence of local intense shear layers as the common basic issue. In order to continue to explore the simple temporal problem, as

well as to render credible certain concepts derived from the present computational results and presented in later sections, we place particular emphasis in the present section on quantitative comparisons with experiments (e.g. Swearingen & Blackwelder 1987; Ito 1985; Aihara & Koyama 1982). However, we have not carried out such comparisons exhaustively. The Görtler instability measurements on the concave side of an air foil (Dagenhard & Mangalam 1986; Mangalam *et al.* 1985) involve local changes in the surface radius. In order to carry out the temporal analogy to this problem, the radius then must be made time dependent. Although this analogy is certainly possible, it is felt that for comparisons with experiments in such problems, the case of a spatial calculation would be more appropriate. Görtler disturbance measurements were made by Petitjeans, Peerhossaini & Wesfreid (1990) in the same water channel as that used by Peerhossaini & Wesfreid (1988), using laser-Doppler anemometry. Comparisons with their data would prove to be of interest after more precise experimental conditions have become available and the sidewall effects are fully assessed.

In the comparison with spatially developing experimental measurements, we have already mentioned that U_c is a free parameter. As it turns out in the following comparisons, a 'universal' $U_c \approx 0.644U_0$ appears to give the best fit with experimental data. The value $0.644U_0$ is relatively close to the value of the streamwise velocity in the Blasius boundary layer in the vicinity of the displacement thickness. Conceivably this might be taken as a 'universal' advection speed in an Oseen-like approximation. However, a possible universal U_c must be regarded as empirical at this stage.

5.1. *Comparison with Swearingen & Blackwelder* (1987)

Swearingen & Blackwelder (1987) used smoke-wire visualization and multiple-probe hot-wire rakes to study the development of longitudinal vorticity elements on the concave side of a curved wind tunnel. The radius of curvature was maintained at a constant $R = 3.20$ m, with a free-stream velocity of $U_0 = 5$ m/s. The spanwise wavelength peculiar to the set of longitudinal vorticity elements in which the detailed structural measurements were made is $\lambda \approx 1.80$ cm. We use this value as the relevant one in the computations (rather than their averaged value of $\lambda \approx 2.30$ cm). The imposition of upstream initial conditions corresponds to the location $X = X_0 =$ 60 cm from the leading edge of the curved section. In this case, the normal, viscous diffusion lengthscale δ_0, here defined as $(\nu X_0/U_0)^{\frac{1}{2}}$, is $\delta_0 = 0.132$ cm (i.e. $Re_{X_0} = 2.055 \times 10^5$ and $Re_{\delta_0} = 453$). This then gives the following dimensionless parameters used in the computations: $G_{\delta_0} = 9.22$, $\alpha\delta_0 = 2\pi\delta_0/\lambda = 0.462$. Of course, the particular Görtler and wave numbers based on δ_0 can be related to the same numbers using the momentum thickness (θ_0) or displacement thickness (δ_0^*) as lengthscales via the local Blasius relations $\delta_0^* = 1.7208\delta_0$, $\theta_0 = 0.664\delta_0$. Here, $G_{\theta_0} = 4.99$ and $\alpha\theta_0 = 0.308$.

The initial amplitude of the disturbance is fixed by the maximum value of the spanwise root mean square of streamwise velocity measurements (Swearingen & Blackwelder 1987), which at $X_0 = 60$ cm is $0.12U_0$. This corresponds to an initial disturbance kinetic energy content across the boundary layer of about $0.018\delta_0 U_0^2$. The comparisons between temporal development (from computations) and spatial development (from experiments) were carried out for an advection velocity $U_c \approx 0.664U_0$. This value was chosen after different trials until good agreement with the experimental streamwise development was reached.

The computations were carried out with the dimensionless form of equations (3.10)–(3.12), the boundary (3.14)–(3.16) and initial conditions, although com-

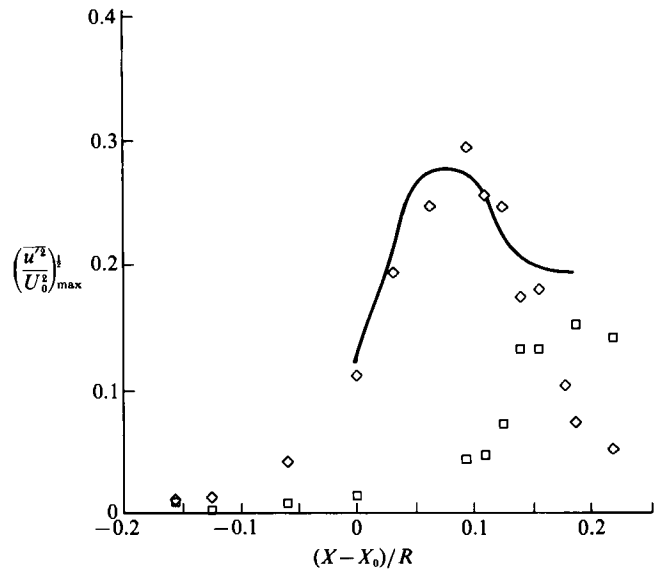

FIGURE 1. Comparison of the downstream development of streamwise-velocity fluctuation maxima: ——, present computed results; ◇, experimental results for steady longitudinal vorticity elements (Swearingen & Blackwelder 1987); □, unsteady contributions. Computational parameters (corresponding to experiments), applied at $X_0 = 60$ cm ($\delta_0 = (\nu X_0/U_0)^{\frac{1}{2}} = 0.132$ cm), $R = 3.20$ cm, $U_0 = 5$ m/s, $(\overline{u'^2})_{\max} = 0.12U_0$.

parisons with experiments are at times given in the dimensional form in which the original data were presented.

5.1.1. *Maximum amplitude development*

In figure 1 we compare the development of the computed maximum disturbance streamwise velocity, in terms of its root-mean-square value (r.m.s.), with the measurements of Swearingen & Blackwelder (1987). The computed streamwise velocity is the total value, that is, the sum of the spanwise-independent mean velocity and the disturbance velocity. The mean velocity is recovered after the computations are performed via the usual Reynolds averaging procedure (which here is the spanwise average). The streamwise disturbance velocity is then obtained by subtracting the mean velocity from the computed total streamwise velocity. The r.m.s. value of the computational results is the spanwise mean. In terms of the translation to the interpretation of the spatial problem, the computational results address only the steady longitudinal vorticity elements.

The measured disturbance development is not entirely free from fluctuations in time. In this case, the time-averaged signal captures the spanwise-dependent 'steady' disturbance characteristic of spatially developing longitudinal vorticity elements originating from upstream Görtler vortices. The time-dependent fluctuations are obtained via subtraction of the steady signals from the total. The r.m.s. of fluctuations involves both spanwise and time means.

As shown in figure 1, the initial development of the steady longitudinal vorticity elements is the strongest, as indicated by the diamond-shaped data points from Swearingen & Blackwelder. Figure 1 is plotted in terms of a dimensionless streamwise development variable $(X-X_0)/R$, where X_0 is the location of the initial

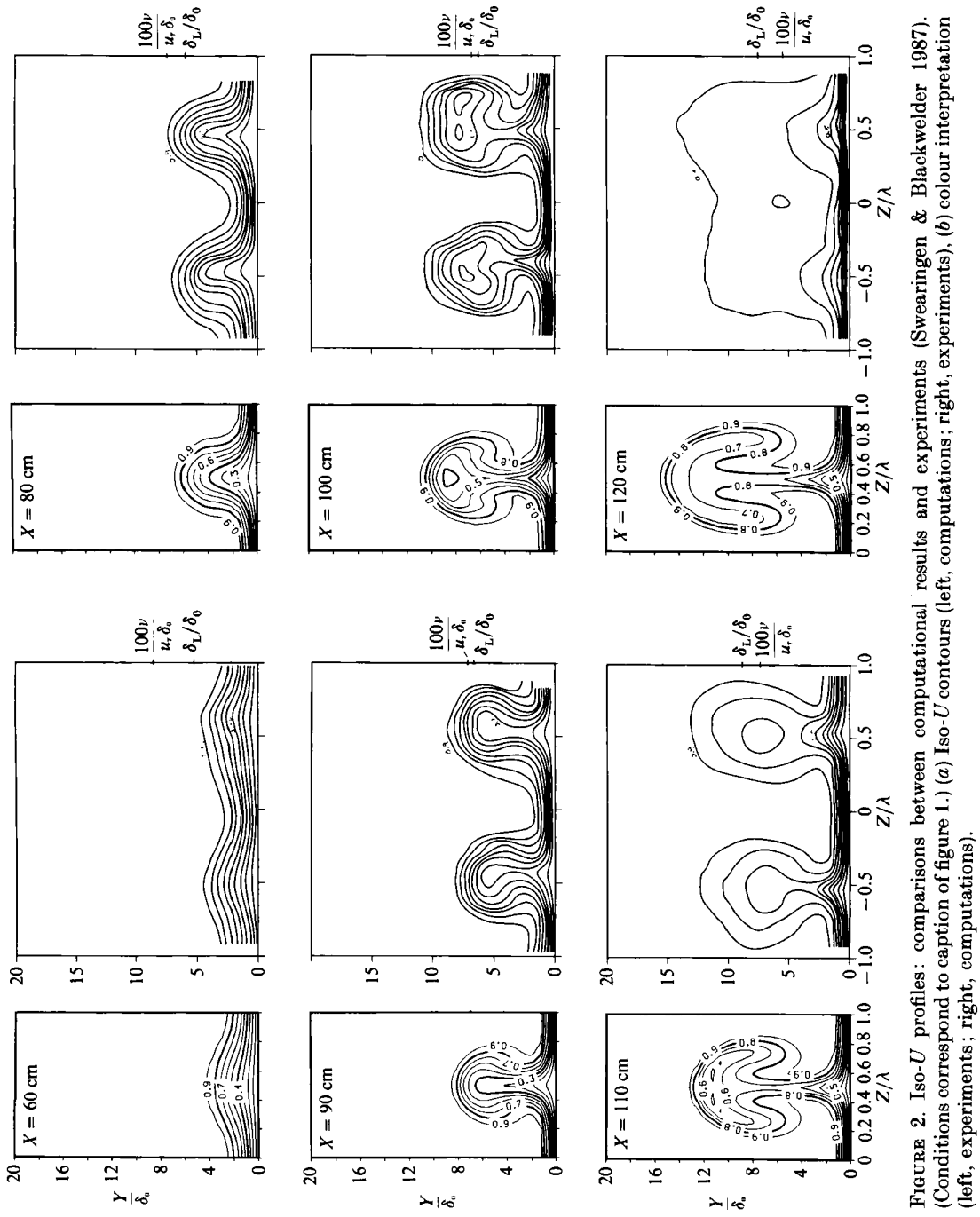

FIGURE 2. Iso-U profiles: comparisons between computational results and experiments (Swearingen & Blackwelder 1987). (Conditions correspond to caption of figure 1.) (*a*) Iso-U contours (left, computations; right, experiments), (*b*) colour interpretation (left, experiments; right, computations).

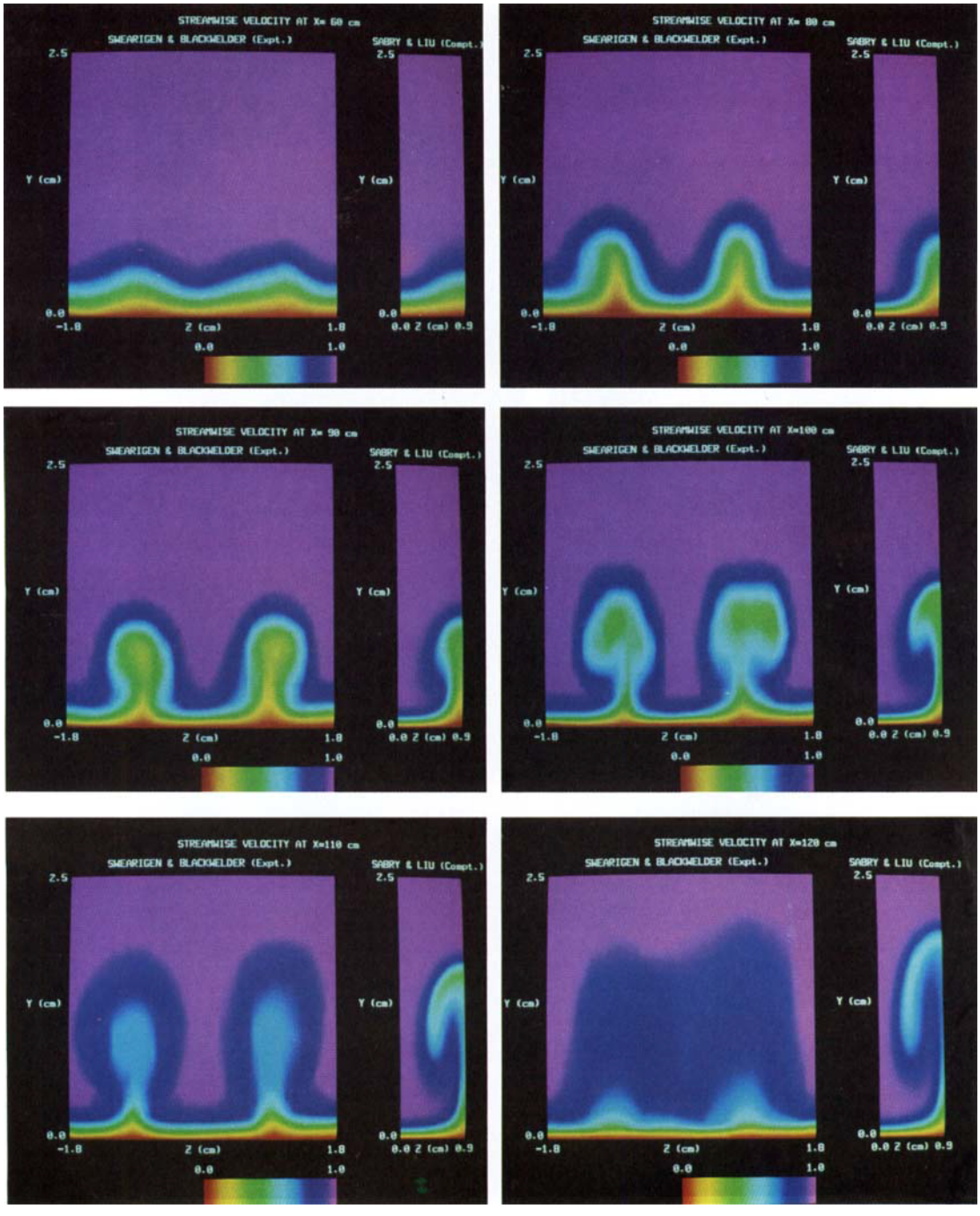

FIGURE 2(*b*). For caption see figure 2(*a*) (facing page).

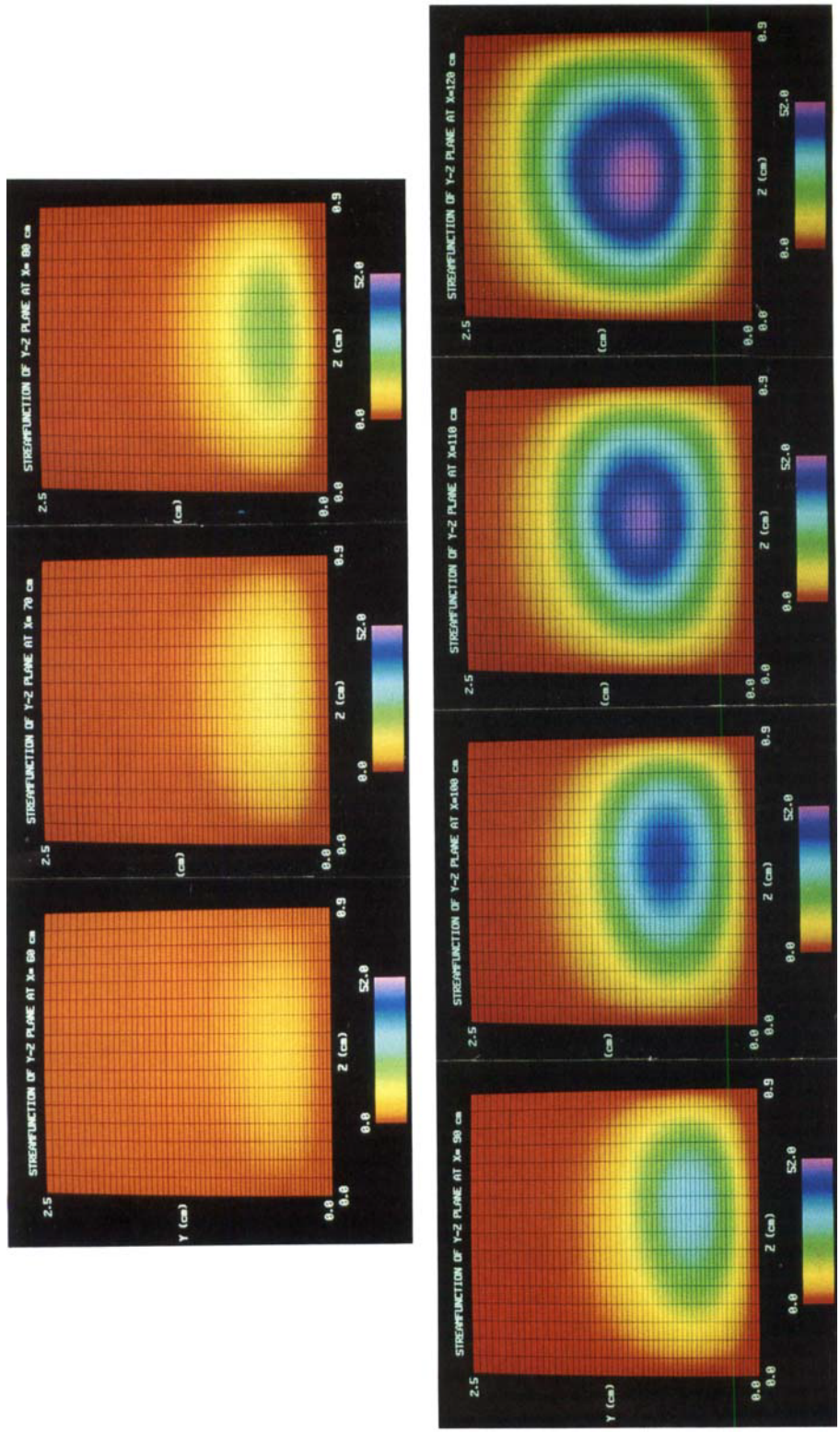

FIGURE 9. Development of the stream function ψ in the (y,z)-plane. (Conditions same as figure 1). *(a)* X=60 cm, *(b)* 70 cm, *(c)* 80 cm, *(d)* 90 cm, *(e)* 100 cm, *(f)* 110 cm, *(g)* 120 cm.

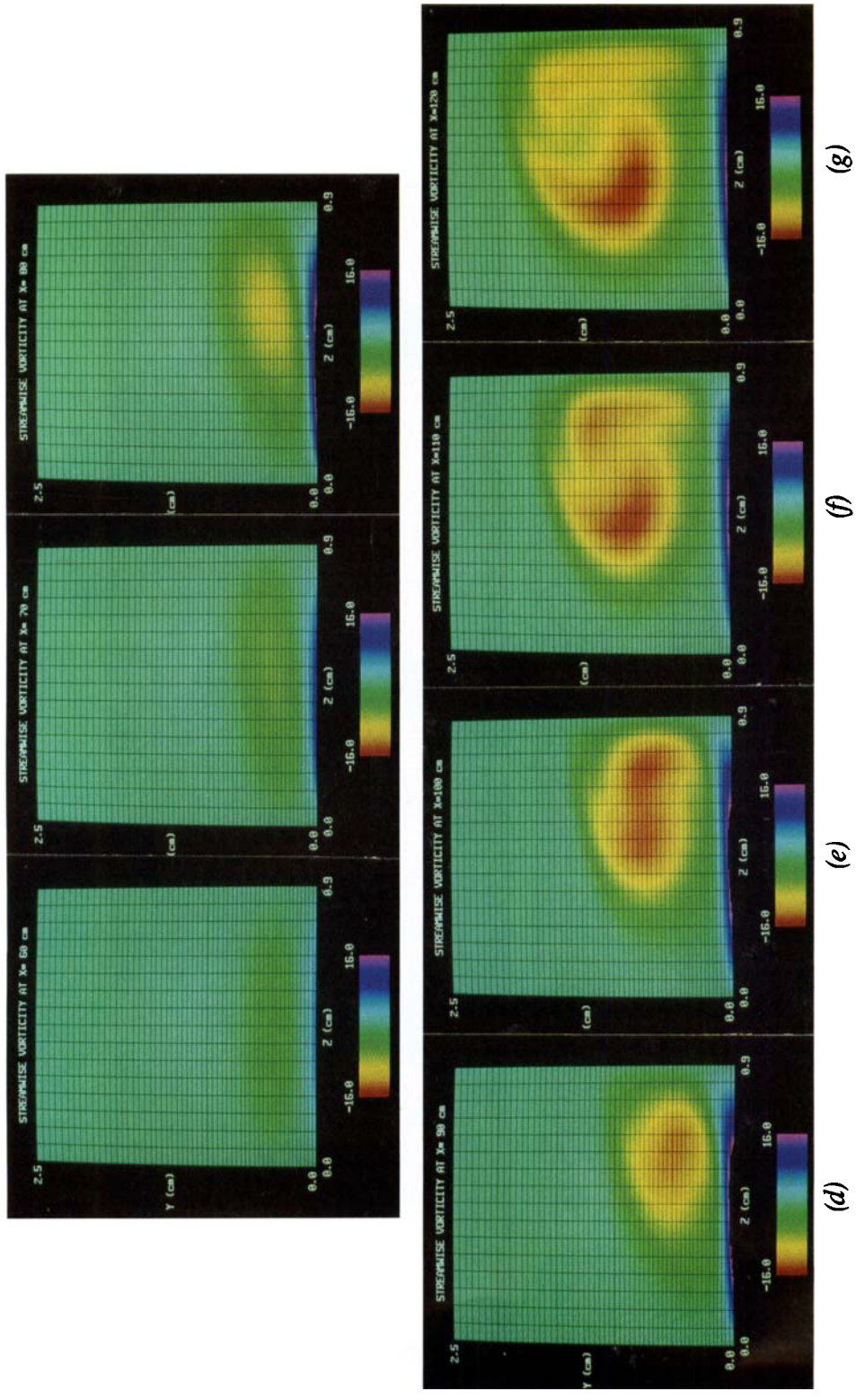

FIGURE 10. Development of the streamwise vorticity magnitude ξ in the (y,z)-plane. (Conditions same as figure 1.) *(a)* X=60 cm, *(b)* 70 cm, *(c)* 80 cm, *(d)* 90 cm, *(e)* 100 cm, *(f)* 110 cm, *(g)* 120 cm.

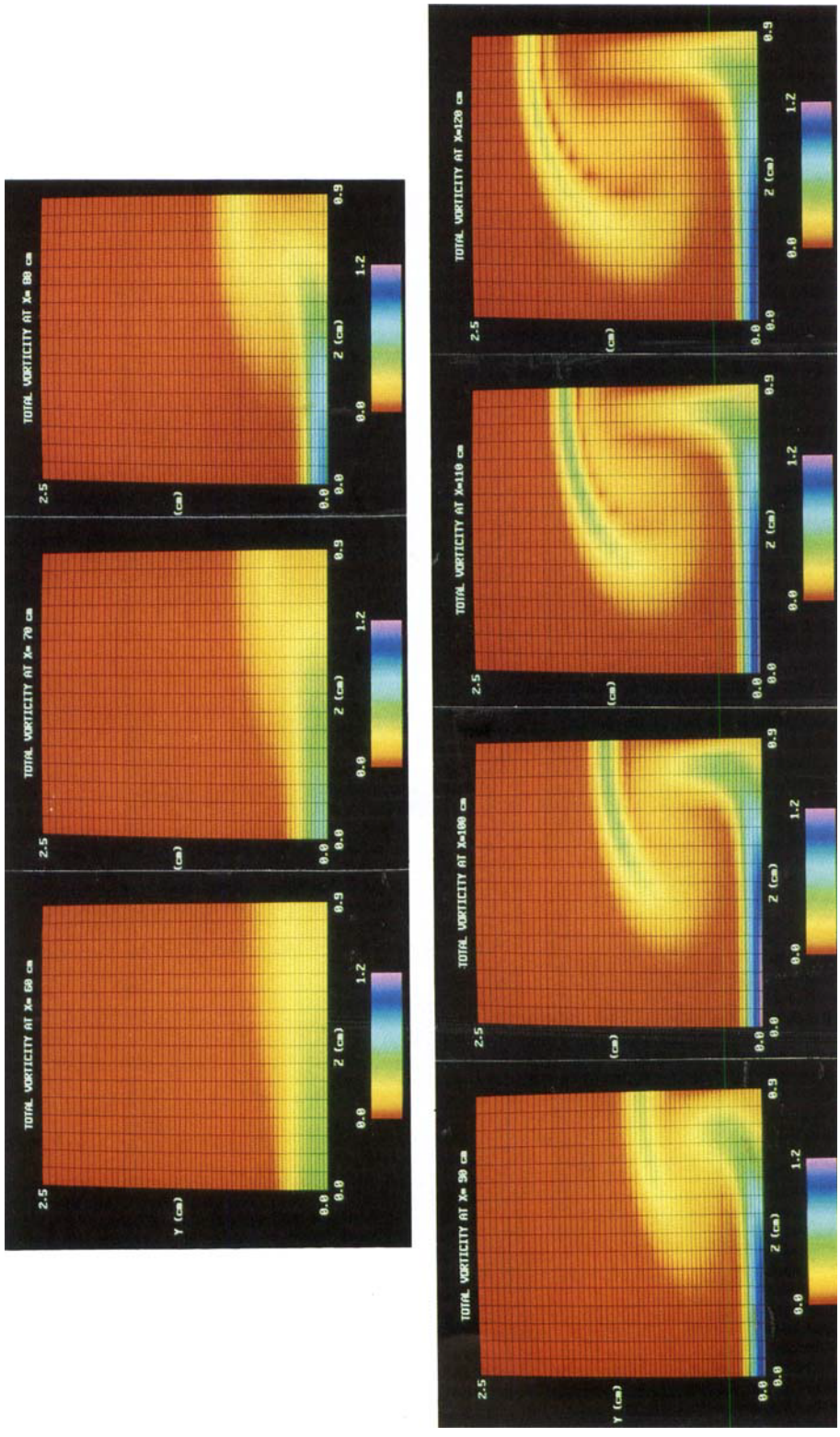

FIGURE 11. Development of the total vorticity magnitude Ω in the (y,z)-plane, contributed predominantly by the vertical and spanwise vorticity magnitudes. (Conditions same as figure 1). *(a)* X=60 cm, *(b)* 70 cm, *(c)* 80 cm, *(d)* 90 cm, *(e)* 100 cm, *(f)* 110 cm, *(g)* 120 cm.

condition in the computations. This emphasizes evolution from initial conditions, in contrast to a plot versus the local Görtler number that still reflects 'local' thinking. The agreement between the computational results and measurements is good, including the growth, peaking and decay, up to where the time-dependent fluctuations in the actual experiment become comparable – in the vicinity of $(X-X_0)/R \approx 0.13$–0.15 ($X \approx 105$–110 cm in the experiments).

While the computational results, which do not take into account the 'dissipative' processes of secondary instabilities and fine-grained turbulence, indicate a 'saturation' downstream, the experimental results show the decay of the longitudinal vorticity elements, while the time-dependent fluctuations (indicated by squares) are strongly amplified owing to the appearance of local, three-dimensional inflexional velocity profiles (to be seen in subsequent figures).

The steady, longitudinal vorticity system that amplifies and decays originated from amplified Görtler vortices in the finite Görtler-number and wavenumber region. The development of secondary instabilities and fine-grained turbulence from such strongly amplified longitudinal vorticity systems, which appear to begin in the vicinity of $(X-X_0)R = \approx 0.1$, has been studied elsewhere (Sabry, Yu & Liu 1989; Yu & Liu 1991).

5.1.2. *Streamwise velocity contours in the cross-sectional plane*

The contours of the total, steady streamwise velocity were obtained by Swearingen & Blackwelder (1987) by using a multiple-probe hot-wire rake. The data were time-averaged in order to recover the time-independent but spanwise-periodic longitudinal vorticity elements that developed from upstream Görtler vortices. These elements are shown on the right in figure 2(*a*). The measurements were made over two spanwise wavelengths 2λ ($\lambda \approx 1.80$ cm), indicated by the Z-axis. The Blasius laminar boundary-layer thickness is indicated by δ_0 on the vertical axis, as is the viscous lengthscale $\nu/u_\tau\delta_0$.

The computational result for the total streamwise velocity is shown on the left of figure 2(*a*) in terms of a one-wavelength domain. The computational iso-U contours are presented in $0.10U_0$ increments, as are the measurements. The initial conditions at $X = 60$ cm show a similar spanwise structure between computationally imposed and measured contours. This similarity, which is quantitative, persists downstream. The iso-U contours described by (3.10) are advected upwards at the 'peak' region ($Z = 0.9$ cm in the computations) and downwards at the 'valley' ($Z = 0$ cm in the computations). Consequently, as seen in figure 2, erupting mushroom-like structures of low-valued U-contours develop surrounding the peak region. This is in accordance with the kinematic picture presented by Stuart (1965) and envisioned by Prandtl (1934).

The striking resemblances hold until about $X = 110$ cm, where detailed hot-wire measurements indicate the presence of secondary instabilities and the further breakdown of the flow into fine-grained turbulence. These mechanisms are not included in the present computations. The large vertical region of nearly constant U in the experiments at $X = 120$ cm indicates the near-establishment of the turbulent boundary-layer profile, with remnants of the spanwise modulation.

Consistent colour interpretations were made of the present computational contours and of our interpretation of the experimental contours taken directly from the paper of Swearingen & Blackwelder (1987). The colour-graphics interpretation of the iso-U contour comparison shown in figure 2(*b*) (plate 1) complements the contour comparisons of figure 2(*a*). The erupting mushroom-like iso-U contours strongly

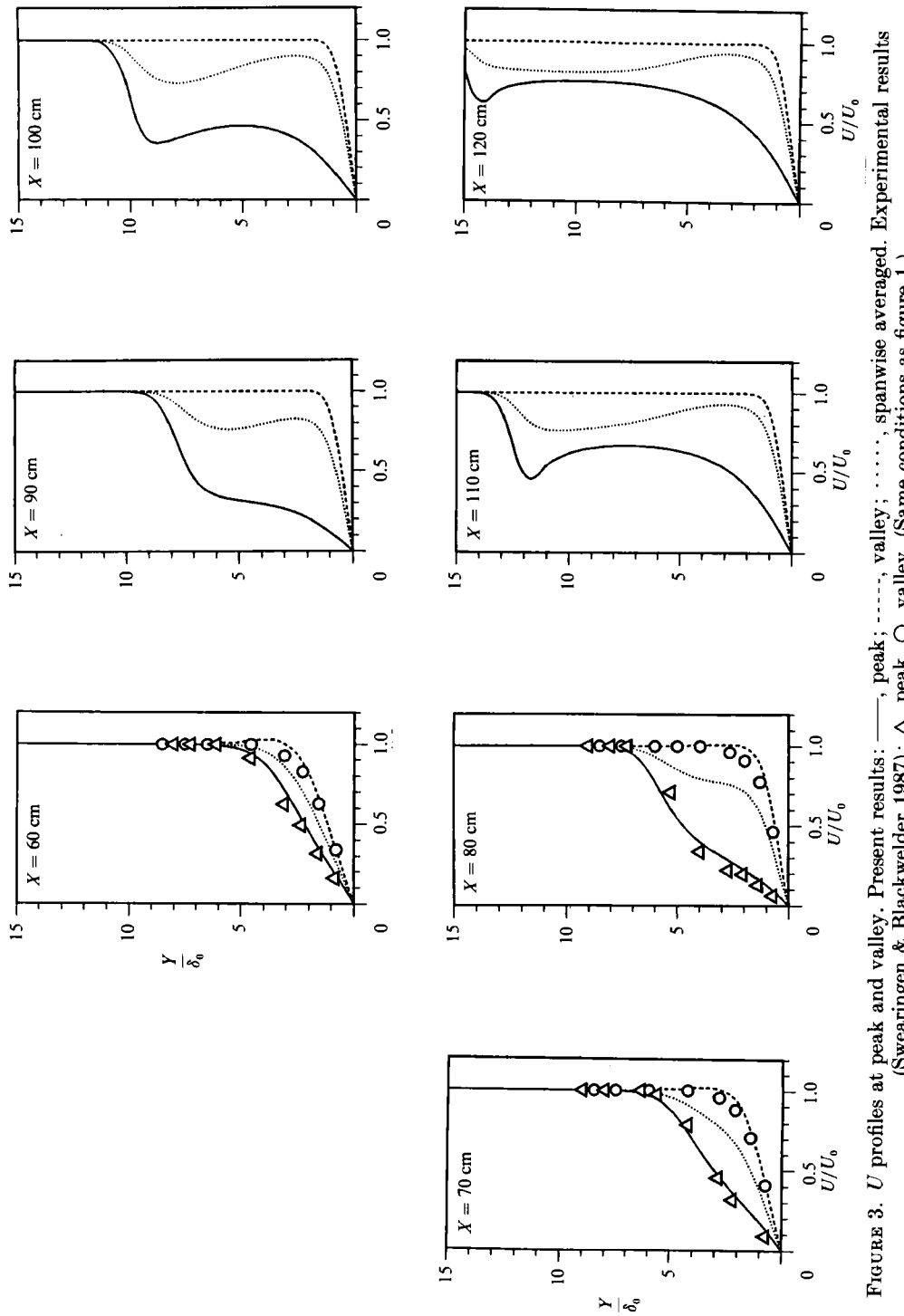

FIGURE 3. U profiles at peak and valley. Present results: ——, peak; - - - -, valley; · · · · ·, spanwise averaged. Experimental results (Swearingen & Blackwelder 1987): △, peak, ○, valley. (Same conditions as figure 1.)

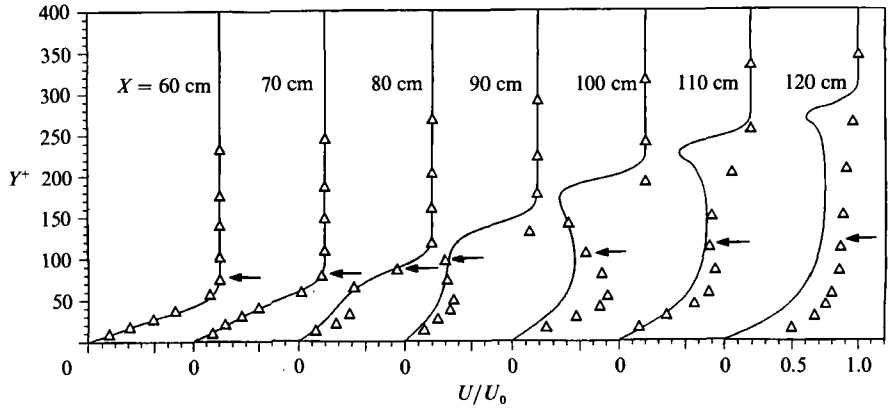

FIGURE 4. Development of U profiles in the peak region. (same conditions as figure 1): ——, present results; △, experimental results (Swearingen & Blackwelder 1987). Arrows indicate Blasius boundary-layer thickness.

resemble the flow visualization studies of the advected-species concentration profiles by Aihara *et al.* (1985), Ito (1985) and Peerhossaini & Wesfreid (1988).

5.1.3. *Development of peak- and valley-streamwise velocity profiles*

To bring out the details of the 'peak' and 'valley' regions, we compare in figure 3 the computational streamwise velocity profiles in such regions with experiments (Swearingen & Blackwelder 1987) as functions of the vertical distance from the wall. The peak region, also commonly called the low-speed region, shows the development of inflexional, total streamwise velocity profiles because of the upwelling activity of the longitudinal vorticity elements. In the valley region, or the high-speed region, the streamwise velocity is higher near the wall because of the downwelling of longitudinal vorticity elements. The comparisons with experimental measurements are in good agreement, again, up to the vicinity of $X \approx 100$ cm where the time-dependent secondary instabilities and turbulence become comparable with the primary disturbance (see figure 1).

The computational result is further spanwise-averaged to produce a mean flow that would correspond to the two-dimensional Blasius velocity profile upstream, as also seen in figure 3. The downstream distortion of such a mean profile to involve two-dimensional inflexion high-shear layers is apparent after $X \approx 80$ cm.

In both the spanwise local structure (figure 2) and the mean profile (figure 3), it is clear that the inflexional profile is intensified and lifted upwards as the flow develops. This is more apparent in the plot in figure 4 of the peak-region profiles as they develop downstream. The normal distance is rescaled by the wall variables ν/u_τ, as suggested by Blackwelder (1983). In this case, the inflexional region 'propagates' rapidly out of the otherwise Blasius boundary-layer region (indicated by the arrow). Moreover, this propagation reaches an outer region of $y^+ \approx 250$–300 by the time almost fully developed turbulence sets in. Again, the comparison with Swearingen & Blackwelder is good to about $X \approx 100$ cm. The experiments show how the intense high-shear layers are smoothed by secondary instabilities and fine-grained turbulence.

In the present problem, the development of inflexional profiles and the generation of turbulence are non-repetitive events accomplished over an advective timescale $(X-X_0)/U_0$ normalized by the wall timescale ν/u_τ^2 of the order $T^+ \sim 380$. This is

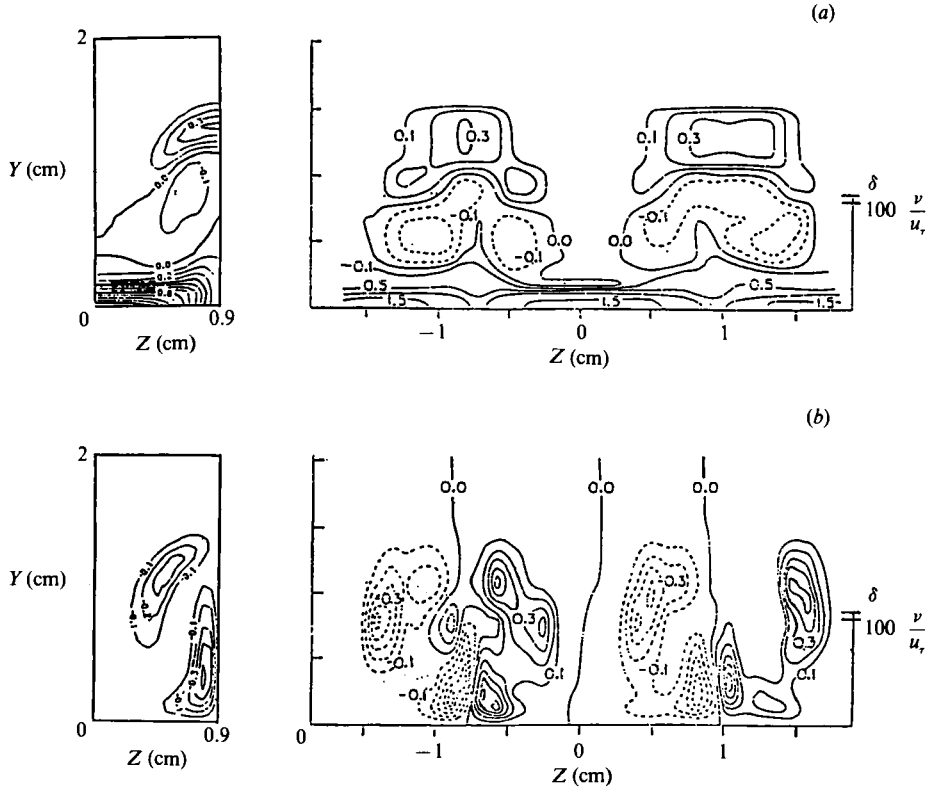

FIGURE 5. Iso-shear ($\sim$ vorticity) contours in the (y,z)-cross-sectional plane at $x = 100$ cm, or $(X-X_0)/R = 0$ (same conditions as figure 1), normalized by spanwise average of $(\partial u/\partial y)_{\text{wall}}$. Computational results are on the left, experiments (Swearingen & Blackwelder 1987) on the right. (*a*) Iso-$\partial u/\partial y$ contours, (*b*) iso-$\partial u/\partial z$ contours.

approximately four or five times longer than the mean bursting period (Kim *et al.* 1971). The shorter period of about $T^+ \sim 90$ takes hold after the establishment of the turbulent boundary-layer profile. On the other hand, in attempts to describe stochastically the presence of 'coherent' structures in turbulent boundary layers, Guezennec, Piomelli & Kim (1989) also observed for a counter-rotating, longitudinal vorticity system, the formation and propagation outwards of the inflexional streamwise velocity profile qualitatively similar to that shown in figure 4. Significant features there are shared with the present problem.

5.1.4. *Normal and spanwise vorticity contours*

We will give a full theoretical discussion of vorticity and enstrophy in §7. Here we compare our computed results with the measured u-velocity derivatives that partially characterize the overall spanwise and vertical vorticities, $\zeta \sim -\partial u/\partial y$ and $\eta \sim \partial u/\partial z$, respectively. The graph on the right-hand side of figure 5(*a*) is taken directly from Swearingen & Blackwelder (1987) for comparison. They also labelled the location of the edge of the unperturbed Blasius boundary layer (δ), as well as the wall units, in terms of ν/u_τ. The computed results, in terms of half wavelengths, are shown on the left-hand side of figure 5(*a*). The comparison is made at $X = 100$ cm in terms of the downstream progress of the nonlinear interactions. The iso-shears here and in figure 5(*b*) are normalized by the Reynolds-averaged local wall shear $\overline{(\partial u/\partial y)_{\text{w}}}$.

The argument between measured and computed contours is rather good. The computed result captures the dimensionless magnitude (≈ 0.3) of the intense spanwise shear in the high-shear layer and its three-dimensional location at about $160\nu/u_\tau$ and in the peak (or node) region. The behaviour of the dimensionless shear near the wall is also captured, ranging from very small in the peak region to more intense towards the valley region.

The intense high-shear layer, carrying $\partial u/\partial y$ maxima in the outer regions of the boundary layer, and the three-dimensional nature of the inflexional region bring great interest to the study of secondary instabilities. The presence of $(\partial u/\partial y)$ peaks is due in no small part to the amplified nature of Görtler vortices initiating upstream at finite wavenumbers. The high inflexional shear (in terms of $\partial u/\partial y$) would be absent in the large-wavenumber limit (Hall & Lakin 1988*a*, *b*; Hall & Seddougui 1989).

The normal vorticity, typified by $\partial u/\partial z$, is shown in figure 5(*b*). The experimental measurements (Swearingen & Blackwelder 1987) are shown on the right and the computational results are on the left. Again, significant experimental features are captured in the computational results. The graphs are shown for the $X = 100$ cm station corresponding to the experiments; the $\partial u/\partial z$ contours are again normalized by $\overline{(\partial u/\partial y)}_w$. The outer region peak in $\partial u/\partial z$, located at about $150\nu/u_\tau$, is about $\frac{1}{2}\pi$ out of phase with the peak region. There is also a peak in $\partial u/\partial z$ at about $30\nu/u_\tau$ in the vicinity of the peak region. The former corresponds to a similar region studied by Hall & Seddougui (1989) for secondary instabilities (in the absence of $\partial u/\partial y$ peaks in the interior of the boundary layer) in the large-spanwise-wavenumber limit. This is more akin to the study of time-dependent instabilities in Taylor–Couette flow (Jones 1981, 1985; Davey *et al.* 1968).

Peak values of $\partial u/\partial z$ and $\partial u/\partial y$ in the high-shear layer region are comparable. It is significant that Blackwelder & Swearingen (1987) showed that the $\partial u/\partial z$ peak distribution correlated better than $\partial u/\partial y$ with the r.m.s. of turbulence oscillations. These suggestions are certainly important for further studies of secondary instability and breakdown in the simultaneous presence of both $\partial u/\partial y$ and $\partial u/\partial z$ peaks in the boundary layer (Sabry *et al.* 1989). The details leading to such intense local free-shear regions are discussed in §8.

5.1.5. *Displacement thickness and skin friction development*

The displacement thickness δ^*, based on the total u-velocity, is computed from the numerical results at the peak and valley regions. The comparison with experiments (Swearingen & Blackwelder 1987) is shown in figure 6(*a*). The agreement with measurements is good throughout the region in which the present computations are valid ($X \approx 100$ cm). The computations recover the observed maximum in δ^* in the peak region, but at a slightly delayed streamwise location ($X \approx 100$ cm) compared to that in the measurements ($X \approx 95$ cm). The computational results for the valley region did not recover the minimum. The dominant mechanism for the maximum/minimum is the further breakdown of the boundary layer and an equilibration of δ^* for the peak/valley regions, as indicated by measurements (Swearingen & Blackwelder 1987). However, though converging, the experimental δ^* does not appear to equilibrate to the turbulent boundary-layer value, at least for this integrated quantity.

The behaviour of the skin friction, which is a Reynolds-averaged quantity, is indicated by $(\partial u/\partial y)_w$ and is shown in figure 6(*b*). The computational results for the skin friction at the peak and valley regions show good qualitative agreement with the measurements of Swearingen & Blackwelder (1987). Although somewhat displaced in

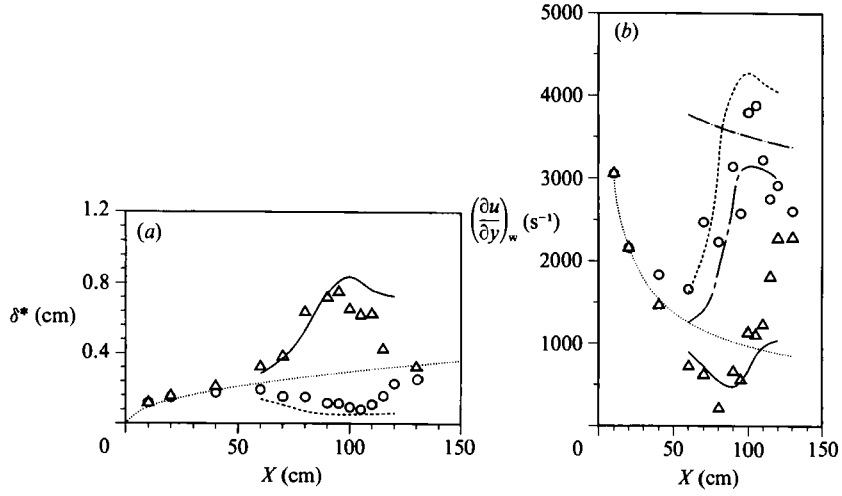

FIGURE 6. Comparison between present computational results and experiments (Swearingen & Blackwelder 1987). (Same conditions as figure 1.) (*a*) Displacement thickness δ^*. Present results: ——, peak; - - - - -, valley. Experimental results: △, peak; ○, valley; · · · · ·, unperturbed Blasius boundary layer. (*b*) Shear stress at the wall $(\partial u/\partial y)_{wall}$. Present results: ——, peak. Experimental results: △, peak; ○, valley; · · · · ·, Blasius boundary layer; —·—, turbulent boundary layer, flat plate; ———, spanwise average.

magnitude, the maximum for the valley and the minimum in $(\partial u/\partial y)_w$ for the peak region occur in the vicinity of the measurements. After Reynolds-averaging the computational result, the mean skin friction appears to a large extent to bridge the Blasius skin friction and the flat-plate turbulent boundary-layer value. Because of this, the present, greatly simplified studies of the nonlinear development of the relevant monochromatic component of longitudinal vorticity appear to be of considerably more interest than anticipated. Further studies of breakdown remain to be made in order to bridge the remaining gap with the turbulent boundary-layer skin friction.

5.2. *Comparison with Ito* (1985)

The experimental conditions of Ito (1985) correspond to the following parameters. The wall radius of curvature was maintained at $R = 1$ m, the free-stream velocity was $U_0 = 2.5$ m/s and the spanwise wavelength of the initial Görtler vortices was $\lambda \approx 1.6$ cm. The initial conditions of the computations were started at $X_0 = 50$ cm, where the maximum amplitude of the streamwise velocity is $0.13U_0$, for which $\delta_0 = 0.171$ cm, $Re_{X_0} = 0.856 \times 10^5$ and $\Lambda_\lambda = 346.5$; $G_{\theta_0} = 5.76$ and $\alpha\theta_0 = 0.446$ ($G_{\delta_0} = 10.65$, $\alpha\delta_0 = 0.672$) and $\Lambda_\lambda \approx 345$ places the initial disturbance in the amplified region according to the linear theory.

Figure 7 presents the comparison with Ito's (1985) measurements of the peak and valley streamwise velocity profiles. The comparison again shows good agreement in the nonlinear development stage of the longitudinal vorticity elements prior to their breakdown. The computational results again show a 'rapid' outward movement of the inflexional profile in the peak region, characteristic of the uplift of the horseshoe vorticity system. The experiments indicate a smoothing of the inflexional profile at about $X \approx 100$ cm, and this must again indicate a secondary breakdown. Further smoothing of the peak and valley profiles is indicated by the measurements (Ito 1985) at $X \approx 100$ cm, although the peak and valley modulation is still discernible.

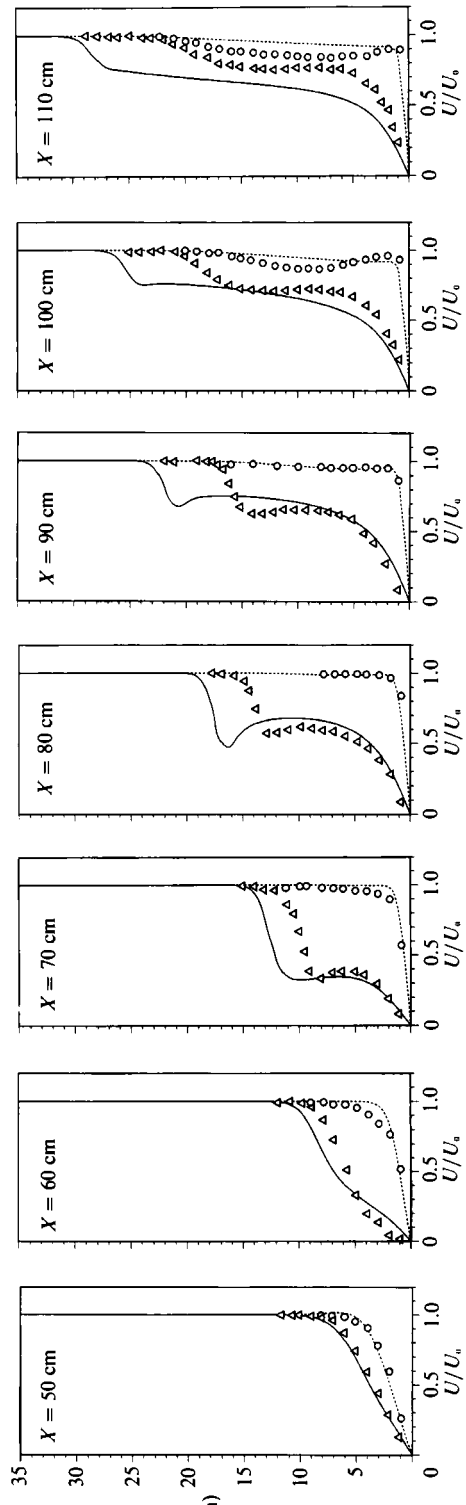

FIGURE 7. Comparison between present computational results and experiments (Ito 1985). Present results: ——, peak; - - - -, valley. Experimental results: △, peak; ○, valley. Computational parameters (corresponding to experiments) applied at $X_0 = 50$ cm ($\delta_0 = (\nu X_0/U_0)^{\frac{1}{2}} = 0.171$ cm), $R = 1$ m, $U_0 = 2.5$ m/s, $G_{\delta_0} = 10.65$, $\alpha\delta_0 = 0.672$, $(\overline{u'^2})^{\frac{1}{2}}_{\max} = 0.12U_0$.

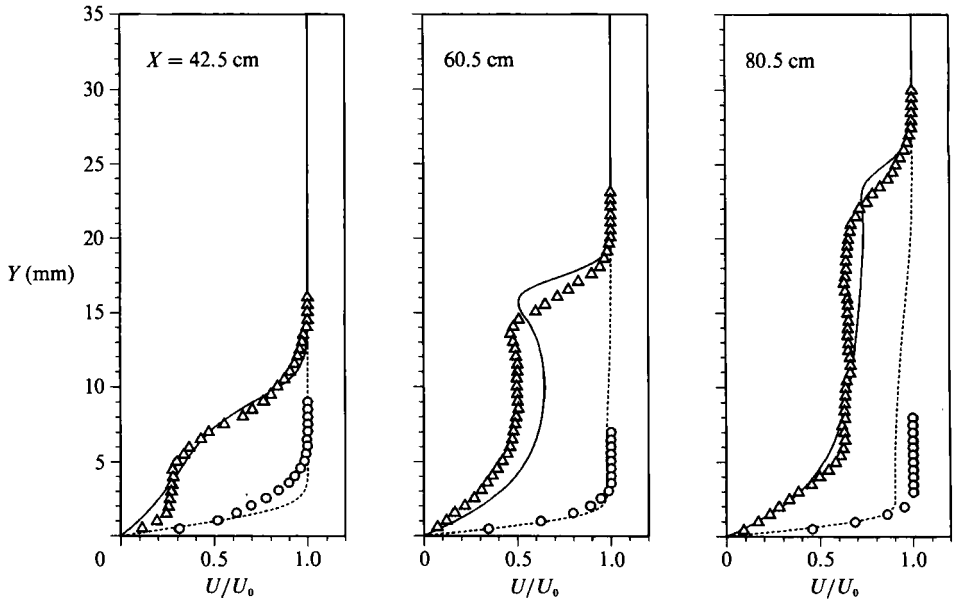

FIGURE 8. Comparison between present computational results and experiments (Aihara & Koyama 1982). Present results: ——, peak; -----, valley. Experimental results: △, peak; ○, valley. Computational parameters (corresponding to experiments) applied at $X_0 = 42.5$ cm ($\delta_0 = (\nu X_0/U_0)^{\frac{1}{2}} = 0.162$ cm), $R = 1$ m, $U_0 = 1.70$ m/s, $G_{\delta_0} = 7.60$, $\alpha\delta_0 = 0.636$, $(\overline{u'^2})^{\frac{1}{2}}_{\max} = 0.128U_0$.

5.3. *Comparison with Aihara & Koyama (1982b)*

Our computations began at the initial location $X_0 = 30.5$ cm, corresponding to Aihara & Koyama's (1982*b*) experiments, for which the maximum streamwise velocity amplitude is $0.128U_0$, with $U_0 = 1.7$ m/s, $R = 1$ m, $\lambda \approx 1.6$ cm, $Re_{X_0} = 3.55 \times 10^4$, $\delta_0 = 0.162$ cm. The initial Görtler and wave number parameters are $G_{\theta_0} = 4.11$, $\alpha\theta_0 = 0.422$ ($G_{\delta_0} = 7.60$, $\alpha\delta_0 = 0.636$) and $\Lambda_\lambda = 235.6$. Again, the initial Görtler vortex is in the amplified region.

The comparison with our computational results is shown in figure 8. The development of three-dimensional inflexional profiles is again confirmed. In these and previous comparisons, the valley region shows a steep, high-velocity profile because of the downward advective motion of the longitudinal vorticity elements. This feature is also obtained in the kinematic calculations of Stuart (1965). The local steep, high-velocity region is somewhat reminiscent of turbulent boundary layers.

6. Stream function and vorticity development

In principle, the stream function ψ given by (3.13) and the streamwise momentum equation (3.10) form a sixth-order system. The stream function is a directly computed quantity. In §5, only those quantities that were measured were shown and compared with experimental results. The stream-function development in the (y, z)-plane, computed for the same conditions as those of §5.1, is shown in figure 9 (plate 2). The rotation is counterclockwise, and the figure shows only one half-wavelength. The peak region is on the right of the figure and the valley on the left. The centre of the initial Görtler vortex is located at one quarter-wavelength in the spanwise location and at about the same physical distance above the wall. As the development proceeds, the centre is lifted upward and towards the peak region to about $X \approx$

100 cm, at which time the centre tends to pull away from the peak and move towards the valley region. Although the secondary instabilities set in at about $X \approx 100$ cm in the measurements (Swearingen & Blackwelder 1987), our computational result nevertheless indicates a transverse 'oscillation' in the (X, Z)-plane. How this is related to the observed (e.g. the flow visualization study in Swearingen & Blackwelder 1987) transverse oscillation associated with a secondary low-frequency instability is not at all clear at this stage. The transverse oscillation of the 'free vortex' (i.e. the ξ component away from the wall) is reminiscent of the Crow instability of trailing vortices.

The system (3.10)–(3.12) was actually used in the computations and the Poisson equation in the (y, z)-plane gives directly the streamwise component of the vorticity ξ in terms of the stream function in the present formulation, $\xi = -\nabla_c^2 \psi$. The streamwise vorticity component is shown in figure 10 (plate 3) as it develops in the cross-sectional (y, z)-plane.

By definition (3.9), $\xi = \partial w/\partial y - \partial v/\partial z$. There is a strong ξ-vorticity source from the wall $(\partial w/\partial y) > 0$ in the interior of the spanwise half-wavelength domain, contributing to the strong $\xi > 0$ in the vicinity of the wall. This is somewhat weakened downstream after uplift of the streamwise vorticity elements. In the interior, the sense of the counterclockwise rotation of the initial Görtler vortex and its subsequent nonlinear development in this domain give the strong $\xi < 0$ contribution. The rotation has the opposite sense in the next symmetrical spanwise half-wavelength domain. The interior streamwise vorticity system is an active one in that it strengthens downstream and is lifted upwards and towards the peak region. The subsequent migration of the streamwise vorticity peak away from the peak region towards the valley region is evident. The computational results actually show the development of two streamwise vorticity peak regions downstream: one near the peak region, the other near the valley region. The one near the peak region is subsequently weakened while the other persists and migrates towards the valley region.

The total vorticity magnitude is obtained from

$$\Omega = (\xi^2/Re + \eta^2 + \zeta^2)^{\frac{1}{2}}. \tag{6.1}$$

The Reynolds-number factor under ξ^2 renders all magnitudes of the vorticity components dimensionless by the same parameters. The developing Ω-contours in the (y, z)-plane are shown in figure 11 (plate 4). In the computational example, $Re = Re_{X_0} = 2.055 \times 10^5$ and typically $\xi \sim O(10)$. The streamwise vorticity contribution is about $|\xi|/Re_{X_0}^{\frac{1}{2}} \approx O(10^{-2})$ to a total $\Omega \approx O(10^{-1})$. Thus, effectively, Ω reflects contributions primarily from $(\eta^2 + \zeta^2)^{\frac{1}{2}}$. The relative weakness of the streamwise vorticity is also noted in experiments (R. F. Blackwelder, private communication, 1988). However, the nonlinear consequences of the streamwise vorticity elements are now shown to be enormous, both theoretically and experimentally.

The uplift of Ω in figure 11 strongly resembles the uplift of the transverse element of the horseshoe vortex system in turbulent boundary-layer observations (Kline *et al.* 1967; Kim *et al.* 1971; Willmarth 1975).

Near the valley region, Ω does not change much as it develops. Near the peak region, however, the effect of vorticity uplift due to v is most evident. Once lifted, vorticity elements are further stretched in the upper regions of the shear layer due to divergence of w in that region. A strong region of concentrated vorticity is thus generated whose intensity reaches a maximum at $X = 100$ cm, corresponding to downstream development in experiments (Swearingen & Blackwelder 1987).

7. Interpretations of vorticity sources: enstrophy

In the present temporal analogy, the streamwise advection mechanism $u\,\partial/\partial x$ is replaced by $\partial/\partial t$ and source mechanisms related to streamwise derivatives are absent. These absent source mechanisms are pointed out here, and those that remain are interpreted. The vortex-stretching mechanism $\xi\,\partial u/\partial x$ is absent in the ξ-vorticity development (see (3.11)). This mechanism would be encountered in a spatially developing flow when the streamwise 'vortex lines' are advected downstream and lifted into regions of higher u in the horseshoe vortex uplift process. (We are indebted to J. T. Stuart for pointing out this mechanism.) The mechanism $-2G^2u\,\partial/\partial z$ in (3.11), which actually comes from the combined effects of vorticity advection and vortex-tilting contributions to ξ, can be reinterpreted as a vortex-tilting mechanism. In its original dimensional form $2G^2u$ is $2U/R$, where U/R is a local particle angular velocity and $2U/R$ is interpreted as a contribution to the spanwise vorticity; this vorticity is tilted towards the streamwise direction by the $\partial U/\partial Z$.

Equations for the vorticity components η and ζ can be obtained similarly to (3.11) as

$$\frac{\partial\eta}{\partial t}+\frac{\partial}{\partial y}\left[-\frac{\partial\psi}{\partial z}\eta\right]+\frac{\partial}{\partial z}\left[\frac{\partial\psi}{\partial y}\eta\right]=-\eta\underbrace{\frac{\partial^2\psi}{\partial y\,\partial z}}_{\text{stretching}}-\zeta\underbrace{\frac{\partial^2\psi}{\partial z^2}}_{\text{tilting}}+\nabla_c^2\eta, \tag{7.1}$$

$$\frac{\partial\zeta}{\partial t}+\frac{\partial}{\partial y}\left[-\frac{\partial\psi}{\partial z}\zeta\right]+\frac{\partial}{\partial z}\left[\frac{\partial\psi}{\partial y}\zeta\right]=\zeta\underbrace{\frac{\partial^2\psi}{\partial z\,\partial y}}_{\text{stretching}}+\eta\underbrace{\frac{\partial^2\psi}{\partial y^2}}_{\text{tilting}}+\nabla_c^2\zeta. \tag{7.2}$$

In the temporal analogy, the tilting mechanisms $-\xi\,\partial^2\psi/\partial x\,\partial z$ and $(-2G^2u\,\partial u/\partial x+\xi\,\partial^2\psi/\partial x\,\partial y)$ are absent from (7.1) and (7.2), respectively. The definitions of the vorticity components η and ζ are further simplified in the temporal problem, (3.9*b*) and (3.9*c*). Of course, one can, if desired, always estimate such mechanisms in terms of the transformation $\partial/\partial t=U_c\,\partial/\partial x$. This estimate would be more meaningful if the actual spatial problem were available for comparison.

In order further to interpret the consequences of vorticity considerations, we split the total vorticity into a Reynolds mean plus a disturbance part,

$$\xi=\xi',\quad \eta=\eta',\quad \zeta=\bar{\zeta}+\zeta', \tag{7.3}$$

where the mean, denoted by an overbar, is obtained via spanwise averaging.

7.1. *Evolution of cross-sectional enstrophy content*

In order to understand the vorticity interactions between the mean motion and the spanwise-varying perturbations, it is appropriate to recast the vorticity components in terms of their respective enstrophy $\overline{\xi'^2}/Re$, $\overline{\eta'^2}$, $\overline{\zeta'^2}$ and $\bar{\zeta}^2$ (see, for instance, Tennekes & Lumley 1972; Liu 1988*a*). The transport equations for the enstrophy are further integrated in the direction normal to the wall, resulting in the time (or approximated streamwise) evolution of enstrophy content in the (y,z) cross-sectional plane. The resulting enstrophy-content evolution equations are

$$\frac{1}{2}\frac{\mathrm{d}}{\mathrm{d}t}\int_0^\infty\frac{\overline{\xi'^2}}{Re}\mathrm{d}y=2\frac{G^2}{Re}\int_0^\infty\underbrace{\bar{u}\overline{\xi'\frac{\partial u'}{\partial z}}}_{\substack{\text{tilting}\\(\xi-1)}}\mathrm{d}y+2\frac{G^2}{Re}\int_0^\infty\underbrace{\overline{u'\xi'\frac{\partial u'}{\partial z}}}_{\substack{\text{tilting}\\(\xi-2)}}\mathrm{d}y$$

$$-\underbrace{\frac{1}{2Re}\frac{\partial\overline{\xi'^2}}{\partial y}\bigg|_{y=0}}_{\substack{\text{flux from wall}\\(\xi-3)}}-\underbrace{\frac{1}{Re}\int_0^\infty\left[\overline{\left(\frac{\partial\xi'}{\partial y}\right)^2}+\overline{\left(\frac{\partial\xi'}{\partial z}\right)^2}\right]\mathrm{d}y}_{\substack{\text{dissipation}\\(\xi-4)}}, \tag{7.4}$$

$$\frac{1}{2}\frac{\mathrm{d}}{\mathrm{d}t}\int_0^\infty \overline{\eta'^2}\,\mathrm{d}y = \int_0^\infty \overline{\eta'^2\frac{\partial v'}{\partial y}}\,\mathrm{d}y + \int_0^\infty \bar{\zeta}\overline{\eta'\frac{\partial v'}{\partial z}}\,\mathrm{d}y + \int_0^\infty \overline{\zeta'\eta'\frac{\partial v'}{\partial z}}\,\mathrm{d}y$$

stretching (η–1) tilting (η–2) tilting (η–3)

$$-\frac{1}{2}\frac{\partial\overline{\eta'^2}}{\partial y}\bigg|_0 - \int_0^\infty \left[\overline{\left(\frac{\partial\eta'}{\partial y}\right)^2} + \overline{\left(\frac{\partial\eta'}{\partial y}\right)^2}\right]\mathrm{d}y. \quad (7.5)$$

flux from wall (η–4) dissipation (η–5)

$$\frac{1}{2}\frac{\mathrm{d}}{\mathrm{d}t}\int_0^\infty \overline{\zeta'^2}\,\mathrm{d}y = -\int_0^\infty \overline{v'\zeta'}\frac{\partial\bar{\zeta}}{\partial y}\mathrm{d}y + \int_0^\infty \bar{\zeta}\overline{\zeta'\frac{\partial w'}{\partial z}}\,\mathrm{d}y + \int_0^\infty \overline{\zeta'^2\frac{\partial w}{\partial z}}\,\mathrm{d}y$$

exchange (ζ–1) stretching (ζ–2) stretching (ζ–3)

$$+\int_0^\infty \overline{\eta'\zeta'\frac{\partial w'}{\partial y}}\,\mathrm{d}y - \frac{1}{2}\frac{\partial\overline{\zeta'^2}}{\partial y}\bigg|_0 - \int_0^\infty \left[\overline{\left(\frac{\partial\zeta'}{\partial y}\right)^2} + \overline{\left(\frac{\partial\zeta'}{\partial z}\right)^2}\right]\mathrm{d}y, \quad (7.6)$$

tilting (ζ–4) flux from wall (ζ–5) dissipation (ζ–6)

$$\frac{1}{2}\frac{\mathrm{d}}{\mathrm{d}t}\int_0^\infty \bar{\zeta}^2\,\mathrm{d}y = +\int_0^\infty \overline{v'\zeta'}\frac{\partial\bar{\zeta}}{\partial y}\mathrm{d}y + \int_0^\infty \bar{\zeta}\overline{\zeta'\frac{\partial w'}{\partial z}}\,\mathrm{d}y$$

exchange ($\bar{\zeta}$–1) stretching ($\bar{\zeta}$–2)

$$+\int_0^\infty \bar{\zeta}\overline{\eta'\frac{\partial w'}{\partial y}}\,\mathrm{d}y - \frac{1}{2}\frac{\partial\bar{\zeta}^2}{\partial y}\bigg|_0 - \int_0^\infty \left[\left(\frac{\partial\bar{\zeta}}{\partial y}\right)^2\right]\mathrm{d}y. \quad (7.7)$$

tilting ($\bar{\zeta}$–3) flux from wall ($\bar{\zeta}$–4) dissipation ($\bar{\zeta}$–5)

The evolution of the cross-sectional perturbation enstrophies in (7.4)–(7.7) is, in general, dictated by the sources or sinks arising from stretching/tilting mechanisms, molecular flux or 'conduction' from the wall due to vorticity sources arising from the no-slip condition, and viscous dissipation, with the exception of $\overline{\zeta'^2}$, which has an enstrophy-exchange mechanism with the mean motion, $\bar{\zeta}^2$, given by the first term on the right of (7.6) and (7.7). This is somewhat analogous to the production mechanism in kinetic energy considerations. The stretching/tilting mechanisms do not give rise to enstrophy-exchange mechanisms.

Equations (7.4)–(7.7) are used to analyse the comprehensive numerical results obtained using parameters corresponding to those in the Swearingen & Blackwelder (1987) experiment. The details of the parameters have already been discussed in §5.1. This numerical example typifies the correspondence of parameters to observations.

The time evolution is again recast into $(X-X_0)/R$ via the Oseen or Rayleigh spatial transformation $t \to x/U_c$ as in §5.1. The evolution of the cross-sectional enstrophy content is shown in figure 12. The enstrophy content associated with the streamwise vorticity $\overline{\xi'^2}/Re$ is an order of magnitude smaller than the normal and spanwise contributions, even as the perturbation amplifies 'downstream'. The mean-motion contribution dominates initially, as would be expected, since the initial

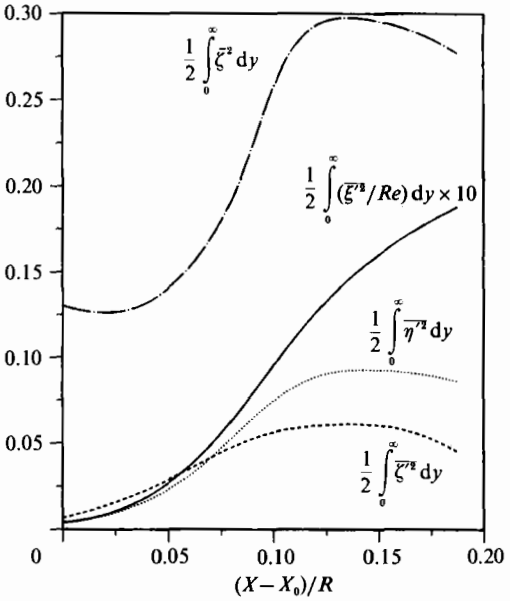

FIGURE 12. Development of mean flow and disturbance enstrophy content. (Conditions same as figure 1.)

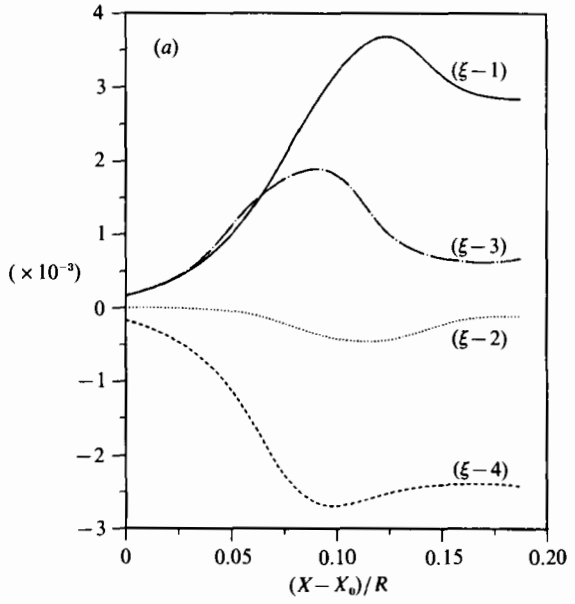

FIGURE 13(*a*). For caption see facing page.

perturbations are generally small. As the flow develops, the sum of the total perturbation contributions becomes of the same order as (though smaller than) the mean-motion enstrophy content. Relative to the dimensional streamwise distance used in the experimental comparisons in §5.1, $X = 80$ cm corresponds to $(X-X_0)/R = 0.0625$, whereas 100 cm corresponds to 0.125, the distance beyond which secondary instabilities are experimentally observed for the present set of initial parameters.

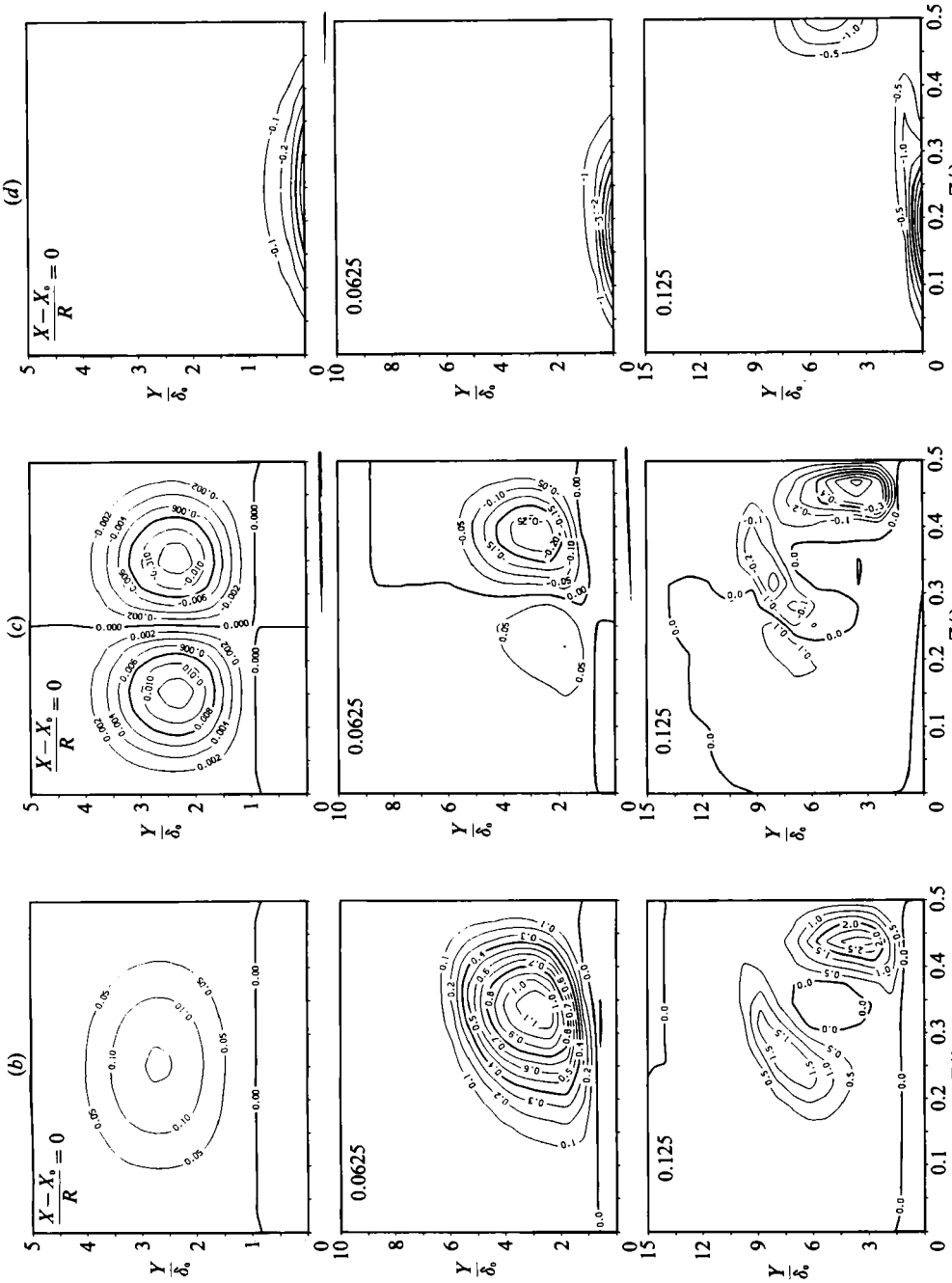

FIGURE 13. Development of the streamwise disturbance enstrophy-content balancing mechanisms (equation (7.4)). (Conditions same as figure 1.) (*a*) Overall balancing mechanisms; (*b*) structural features of $(2G^2\overline{u}\xi'(\partial u'/\partial z))/Re\times10^3$, ($\xi-1$); (*c*) structural features of $(u'\xi'(\partial u'/\partial z))/Re\times10^3$, ($\xi-2$); (*d*) structural features of $[(\partial\xi'/\partial y)^2+(\partial\xi'/\partial z)^2]/Re\times10^3$, ($\xi-4$).

In the following, we illustrate the relative strengths of the balancing mechanisms for integrated, cross-sectional enstrophy development and, for those dominant mechanisms, the evolution of the source or sink distribution in the cross-sectional plane.

7.2. *Evolution of enstrophy balancing mechanisms*

The balancing mechanisms on the right-hand sides of (7.4)–(7.7) for the respective enstrophy content are labelled accordingly. In the following we present the individual mechanisms that give rise to the enstrophy development shown in figure 12.

7.2.1. *Contributions to* $\overline{\xi'^2}$

The cross-sectionally integrated mechanisms for $\overline{\xi'^2}$ evolution are shown in figure 13(*a*). With the terminology introduced in (7.4), the 'tilting' effect from the Görtler mechanism involving the mean flow ($\xi-1$) eventually dominates the sources. The contribution to the ($\xi-1$) cross-sectional integral for this mechanism is shown in figure 13(*b*) as the integrand evolves from its initial distribution according to the (linear) Görtler vortex. This source mechanism intensifies downstream as its 'centre' moves towards the peak region, spreads to the outer regions of the boundary layer and eventually fragments into intense regions (as indicated by the structure of ξ in figure 10).

The 'tilting' mechanism arising from the disturbances u' velocity, ($\xi-2$), has an initial zero contribution, as can be explained by the antisymmetrical behaviour of its detailed structure about the quarter-spanwise wavelength shown in figure 13(*c*). However, the structure of this mechanism evolves to give a predominantly negative contribution to the peak region. Again, fragmentation of the relative intense region is indicated as it evolves downstream in figure 13(*c*).

Although the y-independent spanwise-varying flux from the wall is not shown, its spanwise average ($\xi-3$) is shown in figure 13(*a*) as an important source contribution. Its magnitude is initially similar to that of ($\xi-1$), but it peaks earlier downstream and decays relatively more rapidly.

The contribution to viscous dissipation is shown in figure 13(*d*). Although initially such contributions are confined to the wall region, significant dissipative effects come into play in the peak region as the disturbance amplifies and moves downstream. The cross-sectionally integrated contribution is indicated by ($\xi-4$) in figure 13(*a*). In the region shown, the positive source contributions continue to be larger than the sink contributions, so that

$$\int_0^y \overline{\xi'^2}\,\mathrm{d}y,$$

though 'small' relative to the other contributions to enstrophy, continues to 'amplify'.

7.2.2. *Contributions to* $\overline{\eta'^2}$

The significance of the enstrophy $\overline{\eta'^2}$ is that the vertical vorticity was found experimentally (Swearingen & Blackwelder 1987) to correlate strongly with the sites for secondary instabilities and the generation of turbulence. A study of the details of the sources of $\overline{\eta'^2}$ may well uncover the mechanism for its local intensification. As shown in figure 14(*a*), the sources for the $\overline{\eta'^2}$ content evolution are primarily the stretching and tilting mechanisms (the labelling in figure 14(*a*) corresponds to the right-hand side of (7.5)). The conduction from the wall ($\eta-4$) makes no contribution.

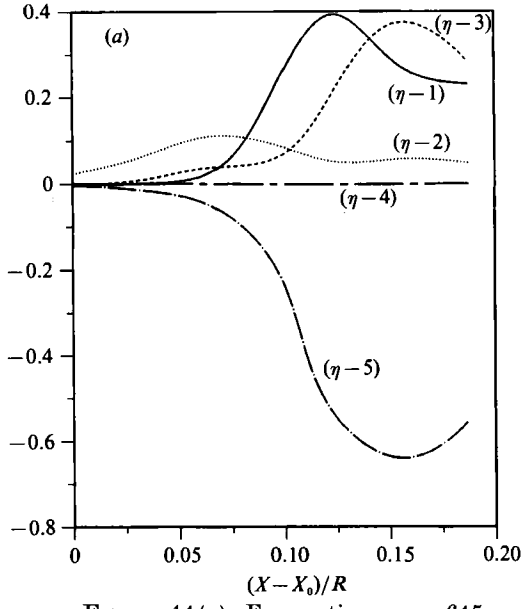

FIGURE 14(*a*). For caption see p. 645.

Initially the tilting of the mean spanwise vorticity $\bar{\zeta}$ is important $(\eta-2)$ and, as the disturbance amplifies, the tilting of ζ' dominates $(\eta-3)$, as does the stretching effect due to the upwelling in the peak region $(\eta-1)$.

The contributions to the third-order stretching $(\eta-1)$ and tilting mechanisms $(\eta-3)$ are initially antisymmetric about the quarter-spanwise wavelength, as shown in figures 14(*b*) and 14(*d*) respectively, and thus they initially integrate to zero. As they develop downstream in figures 14(*b*) and 14(*d*), they intensify towards the peak region. The mechanism of tilting mean vorticity $\bar{\zeta}$ in $(\eta-2)$, though finite initially, becomes obscured by $(\eta-1)$ and $(\eta-3)$ as the disturbance becomes strongly nonlinear downstream.

The viscous dissipation is finite and relatively weak initially (figure 14*e*), but develops into a localized dissipative region immediately about the peak region at about $y^+ \approx 30$. The overall integrated contribution, $(\eta-5)$, 'amplifies' and eventually overcomes the sum of the sources, as shown in figure 14(*a*), leading to the saturation and eventual decay of $\int_0^\infty \overline{\eta'^2}\,dy$ seen in figure 12. However, the $\overline{\eta'^2}$-enstrophy content still remains dominant over $\int_0^\infty \overline{\zeta'^2}\,dy$.

We point out the significant discovery here: that the stretching mechanism $\eta'\,\partial v'/\partial y$ leads to the strong development and intensification of the $\overline{\eta'^2}$-enstrophy source $\eta'^2\,\partial v'/\partial y$ (see figure 14*b*) surrounding the peak region at about $y^+ \approx 30$. This is precisely the region of strong vertical vorticity η' (figure 5*b*) in the inner-boundary-layer region where high-frequency secondary instabilities and eventual breakdown and transition to fine-grained turbulence take place (Swearingen & Blackwelder 1987). Also significant is the observation here that the vorticity-tilting mechanism $\zeta'\,\partial v'/\partial y$ (figure 14*d*), which gives rise to the $\overline{\eta'^2}$-enstrophy source $\zeta'\eta'\,\partial v'/\partial z$, develops into two intense regions (though of a lesser extent than the stretching mechanisms). One of these regions is, again, near the peak region at about $y^+ \approx 30$, and augments the intense source due to the stretching mechanism $\eta'^2\,\partial v'/\partial y$. The other intense region also surrounds, but is further away from, the peak region

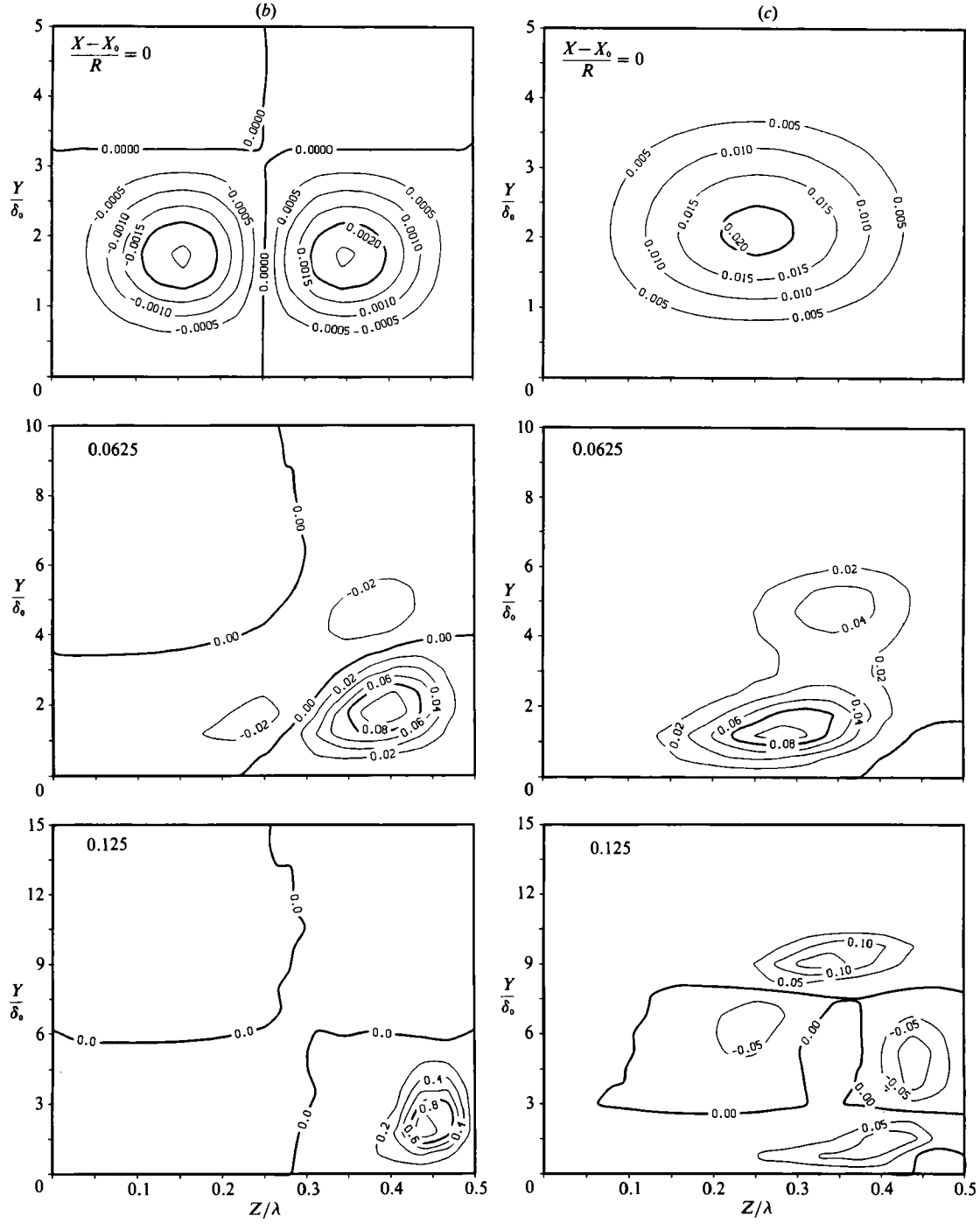

FIGURE 14 (*b*, *c*). For caption see facing page.

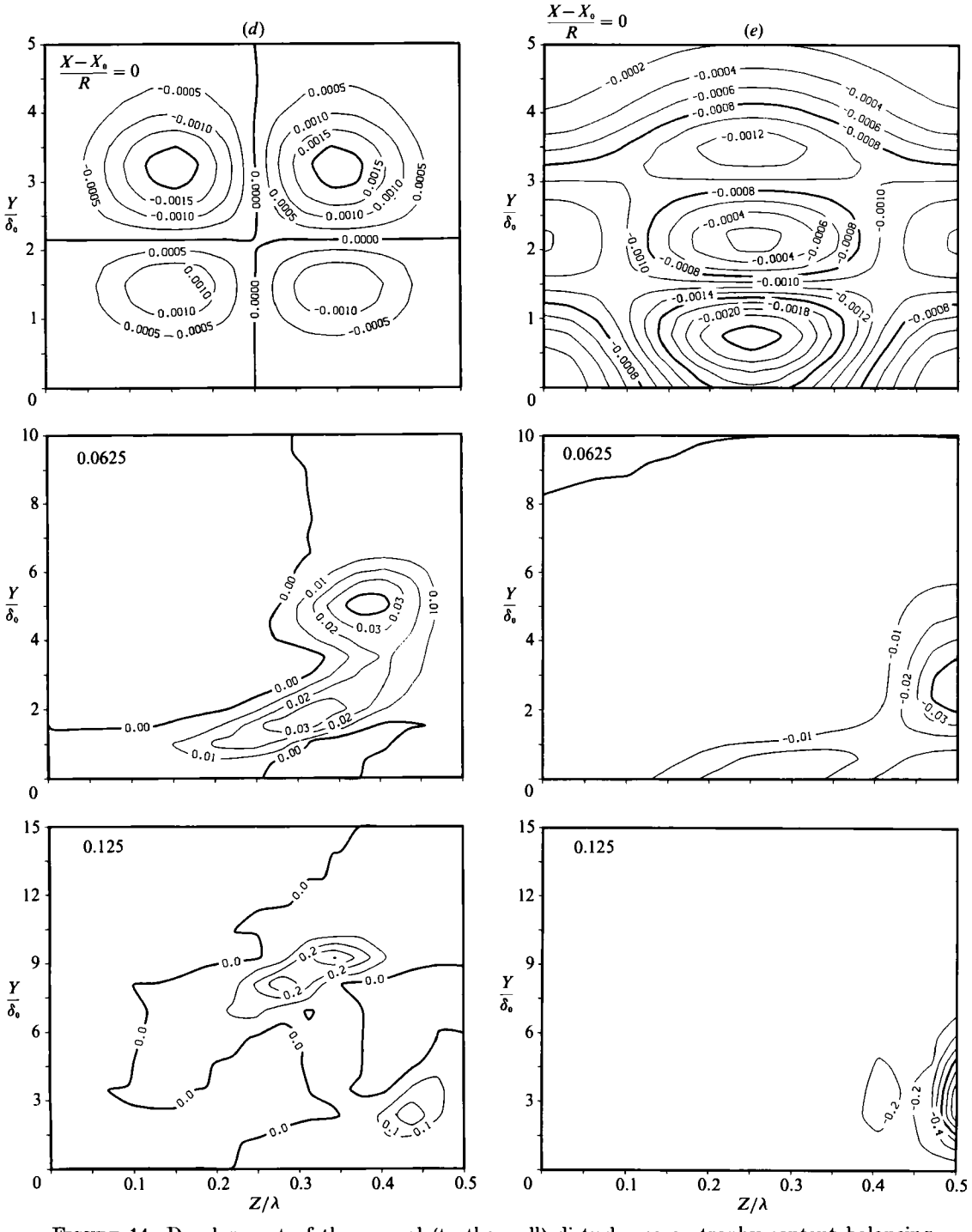

FIGURE 14. Development of the normal (to the wall) disturbance enstrophy-content balancing mechanisms (equation (7.5)). (Conditions same as figure 1.) (*a*) Overall balancing mechanisms; (*b*) structural features of $\eta'^2\partial v'/\partial y$, $(\eta-1)$; (*c*) structural features of $\bar{\zeta}\eta'\partial v'/\partial z$, $(\eta-2)$; (*d*) structural features of $\zeta'\eta'\partial v'/\partial z$, $(\eta-3)$; (*e*) structural features of $(\partial\eta'/\partial y)^2+(\partial\eta'/\partial z)^2$, $(\eta-5)$.

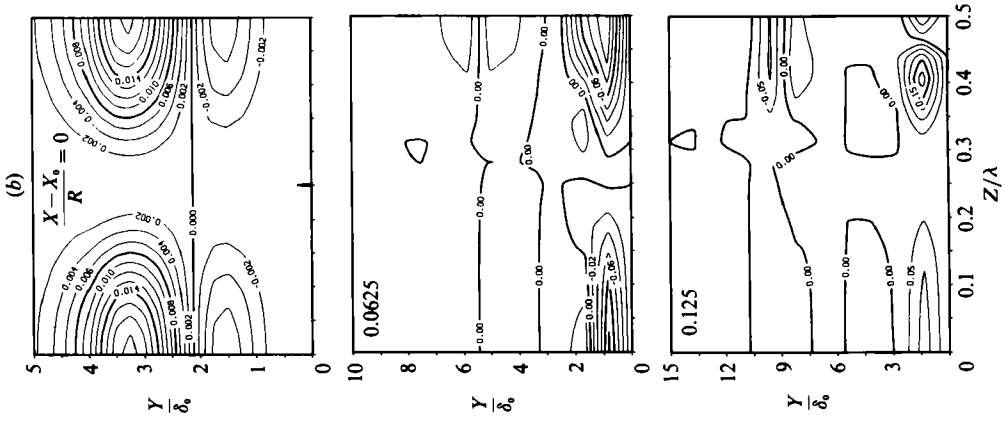
(b)
$\frac{X-X_0}{R}=0$
0.0625
0.125
$\frac{Y}{\delta_0}$
Z/λ

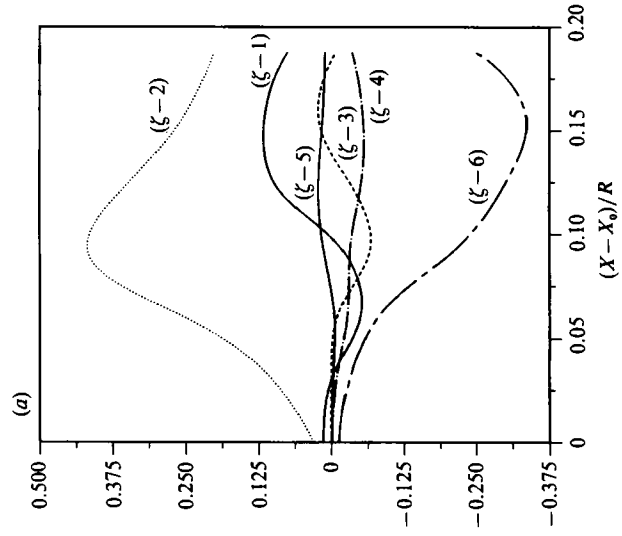
(a)
(ξ−1)
(ξ−2)
(ξ−3)
(ξ−4)
(ξ−5)
(ξ−6)
$(X-X_0)/R$

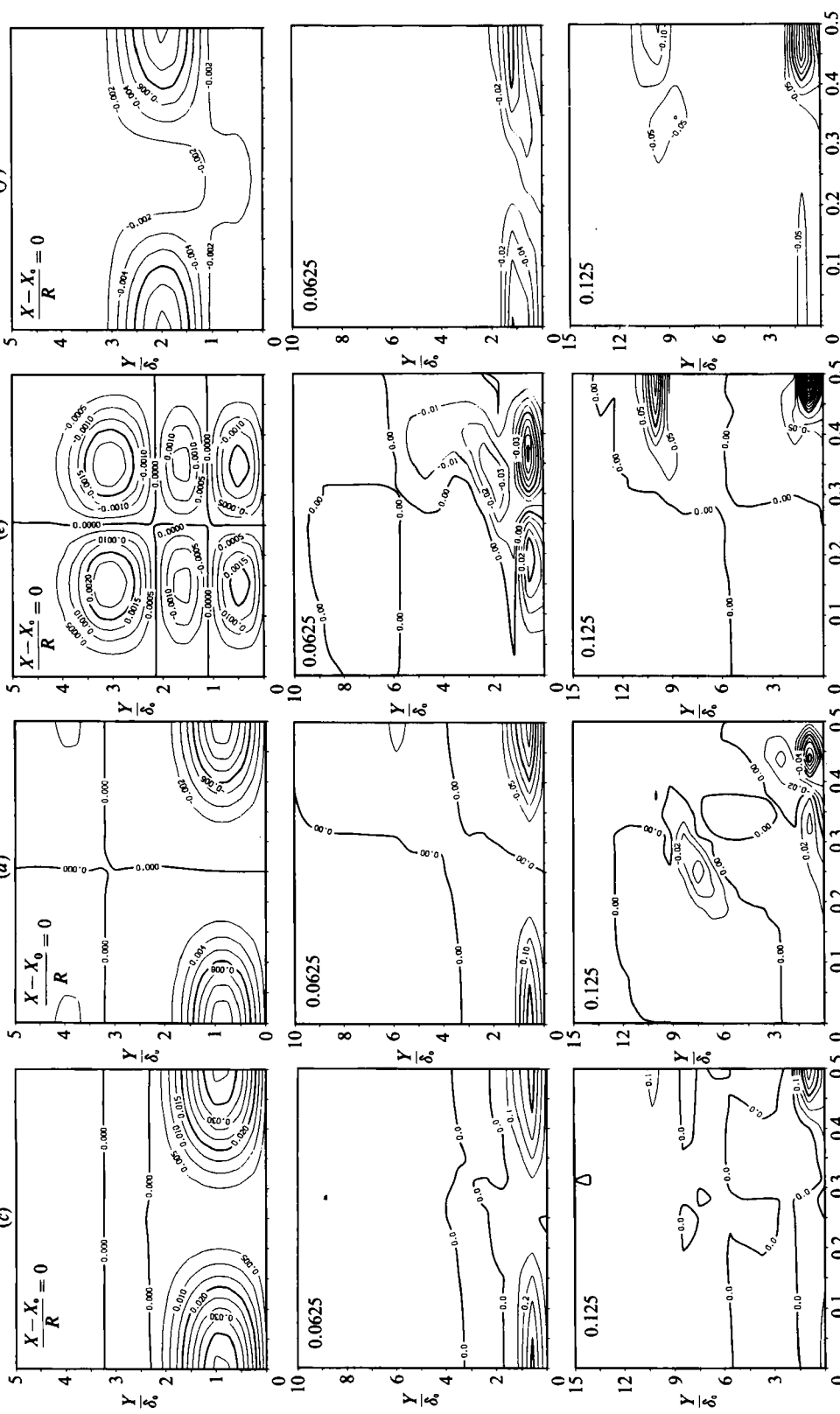

FIGURE 15. Development of the spanwise disturbance enstrophy-content balancing mechanisms (equation (7.6)). (Conditions same as figure 1.) (*a*) Overall balancing mechanisms; (*b*) structural features of $v'\zeta'\,\partial\xi'/\partial y$, ($\xi-1$); (*c*) structural features of $\xi\zeta'\,\partial w'/\partial z$, ($\xi-2$); (*d*) structural features of $\zeta'^2\partial w'/\partial z$, ($\xi-3$); (*e*) structural features of $\zeta\eta'\,\partial w'/\partial y$, ($\xi-4$); (*f*) structural features of $(\partial\xi'/\partial y)^2+(\partial\xi'/\partial z)^2$, ($\xi-6$).

in the outer layer of the boundary layer where sites of initial, weaker secondary instabilities and turbulence development arise (Swearingen & Blackwelder 1987). These two regions correspond to the base and shoulder regions, respectively, of the computed and measured (Swearingen & Blackwelder 1987) mushroom-like iso-U profiles (figure 2).

7.2.3. *Contributions to* $\overline{\zeta'^2}$

Contribution to the perturbation, spanwise enstrophy-content evolution is given in (7.6). It is the only contribution here that exchanges enstrophy with the mean flow through the conversion mechanism $-\overline{v'\zeta'}\,\partial\bar{\zeta}/\partial y$. It is denoted as $(\zeta-1)$ in figure 15(a) and has several oscillations from positive to negative values. The evolving structural features are shown in figure 15(b). We can see that an intense source region is developed in the inner region, close to the peak.

The dominant source for the $\overline{\zeta'^2}$-enstrophy content is the mechanism involving the stretching of mean flow vorticity $\bar{\zeta}$ by the spanwise rate of strain $\partial w'/\partial z$. This is denoted by $(\zeta-2)$ in figure 15(a); its structural evolution is shown in figure 15(c). As far as the enstrophy source is concerned, $\bar{\zeta}\zeta'\,\partial w'/\partial z$ attains maxima at both the inner and outer regions close to the peak (figure 15c).

The accompanying stretching mechanism due to ζ', denoted by $(\zeta-3)$ in (7.6) and figure 15(a), also undergoes positive–negative oscillations, like $(\zeta-1)$. Although its amplitude is relatively small, the cross-sectional structural features, shown in figure 15(d), point to intensification of this source mechanism surrounding the peak in both the outer and inner regions of the boundary layer.

The tilting of η' due to the shear $\partial w'/\partial y$, denoted by $(\zeta-4)$ in figure 15(a) and (7.6), gives rise to a sink for the $\overline{\zeta'^2}$-enstrophy content. Its intensification at the inner region and outer, 'shoulder' region surrounding the peak is noted in figure 15(e).

The overall viscous conduction contribution, shown as $(\zeta-5)$ in figure 15(a), is again not shown here, as it is uniform in z. The overall contribution is much less significant than the source $(\zeta-2)$ and the viscous dissipation $(\zeta-6)$. The detailed structural contributions to the latter are shown in figure 15(f). It evolves from the linear Görtler contribution (figure 15f), which is symmetrical bout $\frac{1}{2}\pi$, towards the isolated regions, with strong dissipation concentrations about the peak region in both the inner and outer region and about the valley in the inner region. The overall contribution of the integrated $\frac{1}{2}\overline{\zeta'^2}$-enstrophy content to the rate of viscous dissipation is as significant as its net source contributions. Saturation for this numerical example is reached at about $(X-X_0)/R \simeq 0.13$ (figure 15a). This is also the vicinity where experiments (Swearingen & Blackwelder 1987) indicate that incipient secondary instabilities occur.

7.2.4. *Contributions to* $\bar{\zeta}^2$

The integrated contributions to $\bar{\zeta}^2$ are shown in figure 16(a). The individual mechanisms identified as $(\bar{\zeta}-1)$ to $(\bar{\zeta}-5)$ in (7.7) are correspondingly indicated in figure 16(a). The exchange mechanism $(\bar{\zeta}-1)$ is just the negative of $(\zeta-1)$ in figure 15(a), and its structural details follow that of $(\zeta-1)$, with a change in sign, in figure 15(b).

The stretching mechanism $\bar{\zeta}\zeta'\,\partial w'/\partial z$ is a mechanism shared also by $\overline{\zeta'^2}$ and is not an exchange mechanism (Tennekes & Lumley 1977; Liu 1988a). The details of $(\bar{\zeta}-2)$ are the same as those of $(\bar{\zeta}-2)$ in figure 15(c), with no change in sign.

The detailed tilting-mechanism contribution indicated by $(\bar{\zeta}-3)$ is shown in figure 16(b). It evolves from a predominantly negative contribution in the outer region,

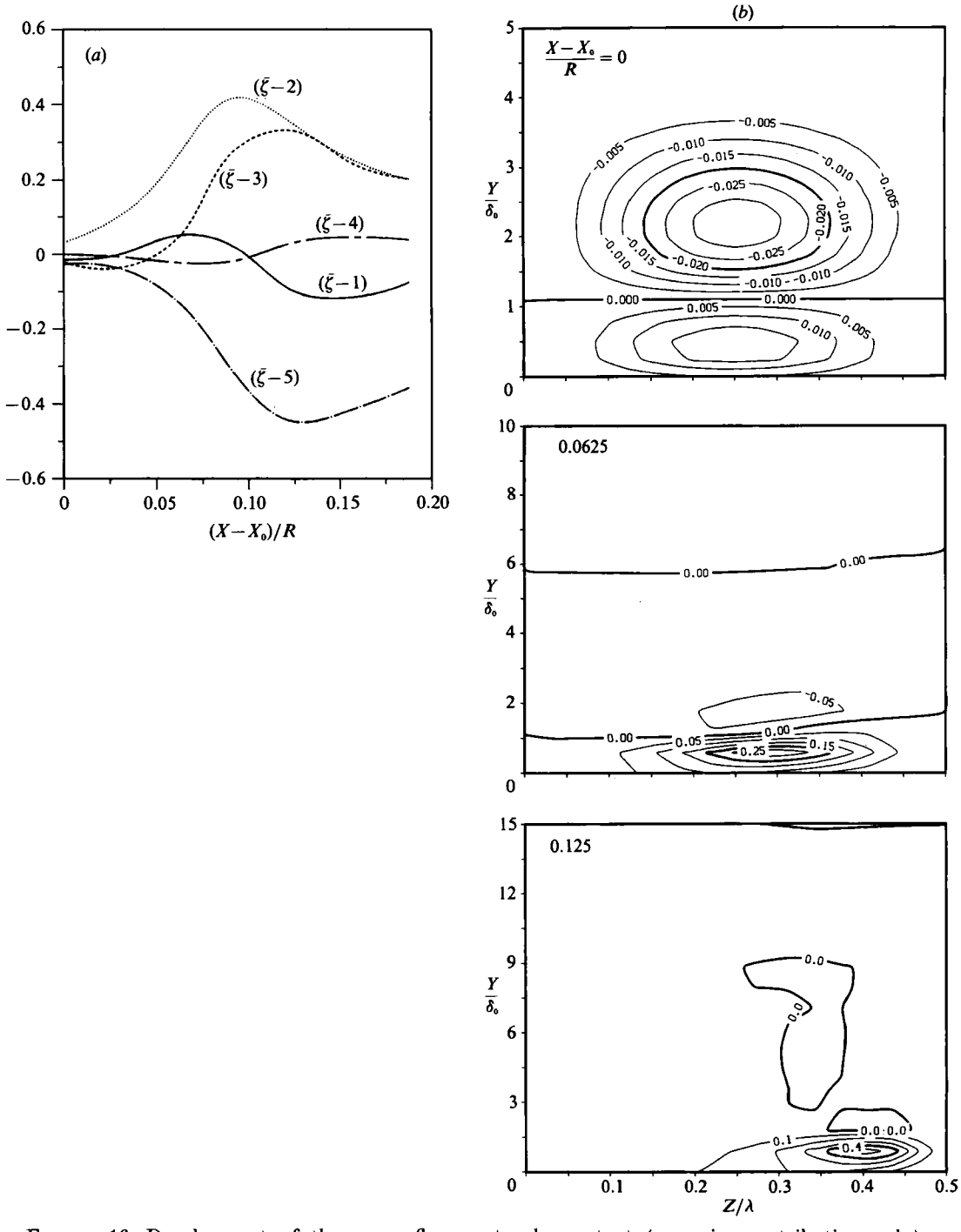

FIGURE 16. Development of the mean flow enstrophy-content (spanwise contribution only) balancing mechanisms (equation (7.7)). (Conditions same as figure 1.) (*a*) Overall balancing mechanisms; (*b*) structural features of $\bar{\zeta}\eta' \partial w'/\partial y$, $(\zeta-3)$.

symmetrical about $\frac{1}{2}\pi$ of the spanwise wavelength region, towards a dominant positive contribution in the inner region surrounding the peak. The overall behaviour evolves from an initially slightly negative contribution (figure 16*a*) towards a positive contribution of similar magnitude to the stretching mechanism ($\bar{\zeta}-2$). The details of both the conduction ($\bar{\zeta}-4$) and viscous dissipation contribution ($\bar{\zeta}-5$) are not shown, since they have no spanwise variations. The former is a weak contribution; the dissipative effects of the latter are concentrated in the inner region, as would be expected and make a dominant contribution in the evolution of $\bar{\zeta}^2$. The shape of

$$\frac{1}{2}\int_0^\infty \bar{\zeta}^2 \,\mathrm{d}y,$$

shown in figure 12, is similar to that of the wall shear-stress evolution shown in figure 6(*b*).

8. Effects of initial conditions

The recognition of the Görtler vortex problem as an initial-value problem in real, developing boundary layers (Hall 1983) certainly suggests the possibility of controlling the flow development via initial conditions. This is reminiscent of the situation in free shear flows where a similar recognition (Liu 1971, 1974) led to many conceptual ideas for its control (e.g. Liu & Kaptanoglu 1987, 1989; Nikitopoulos & Liu 1990).

In this section we give a brief discussion of the effect of 'initial' conditions. The consequential results are presented in terms of (i) the development of total streamwise velocity contours in the cross-sectional plane (the quantitative and qualitative effects of such contours would be measurable); (ii) the cross-sectional stream function (though not measurable, its gradients are related to V, W and ξ); (iii) the skin friction at the wall (also measurable).

We use the numerical example of §5.1 as a standard case to which variations of initial conditions and parameters are compared. The numerical computations are carried out for the same Reynolds number, Re_{X_0}. This implies that the initial conditions are applied at the same streamwise station. We recall that the dimensionless initial streamwise distance X_0/δ_0, because of the definition of δ_0, is just $Re_{X_0}^{-\frac{1}{2}}$. Thus, comparisons between cases of different initial amplitudes, Görtler numbers and wavenumbers are for disturbances imposed at the same initial location and thus are meaningful for such parameter variations. The advection velocity U_c used in the translation between the time-dependent numerical computations and spatially developing flows remains $0.664U_0$, as in the comparisons of different sets of experiments in §5. The variation of initial parameters are tabulated in table 1.

8.1. *Initiated Görtler vortices developing on a straight wall*

In the apparatus of Peerhossaini & Wesfreid (1988) and Peerhossaini (1984, 1985), longitudinal vortices persisted well into the straight section of the water channel (J. E. Wesfreid personal communication, Paris 1988). This certainly suggests that the longitudinal vorticity elements developing from initial Görtler vortices cannot be described by a local theory but must be characterized by a 'rate-controlling' non-equilibrium process that is, as already emphasized, dependent on the initial conditions. The non-equilibrium process here is simply the imbalance between energy supply from the mean motion and viscous dissipation.

The relevant parameters of this straightened-wall case, denoted as Case 1, are

	Λ_λ	G_{0_0}	$\alpha\theta_0$	$[(\overline{u'^2}/U_0^2)^{\frac{1}{2}}]_{\max}$
Standard case (§5.1)	460	5.01	0.308	0.12
Case 1	460	5.01	0.308	0.12
	(but 0 in conservation equations)			
Case 2	230	2.51	0.308	0.12
Case 3	460	5.01	0.308	0.03
Case 4	460	5.01	0.308	0.48
Case 5	1300	5.01	0.154	0.12

TABLE 1. Initial parameters

listed in table 1. Thus G is set to zero in the conservation equations ($\Lambda_\lambda = 0$ is implied). The initial conditions are imposed at the same dimensionless 'streamwise' station $X_0/\delta_0 = Re_{X_0}^{\frac{1}{2}}$. Thus Re_{X_0} is kept constant here (and in all other cases).

The development of the dimensionless total streamwise velocity contours is shown in figure 17. Although the gradient becomes slightly steeper in the valley region, the development of the mushroom-like structure near the peak does not occur. In fact, the gradients decrease near that region. In the range of $(X-X_0)/R$ shown, it is unlikely that sites for secondary instabilities would be present, in contrast to similar profiles of §5.1.

Of interest is the development of the cross-sectional stream function shown in figure 18. We note that there is very little change in the location of the $\psi = 1$ boundary throughout the flow development. However, inside to this $\psi \simeq 1$ boundary, the stream function (and its gradients) are deintensified, leading to a weakening of V, W and ξ. There is practically no shift of the location of $\psi_{\max}$ towards the peak. Such a shift, and the accompanying development of mushroom-like structures, are features of the strong nonlinear processes, as in §5.1, which are absent in the $G = 0$ situation.

The corresponding $\partial u/\partial y$ at the wall is shown in figures 19(*a*), and 19(*b*) for the valley and peak regions, respectively, normalized by the spanwise averaged value at $(X-X_0)/R = 0$. In the valley region, the value of the shear stress at the wall is considerably decreased from its high value in the standard case, due to a weakened downwelling V. In the peak region, where the standard case exhibits a weakened shear stress, the $G = 0$ case shows a slight relative increase; this is because of the weakened V in the upwelling process.

In this numerical example, even when the centrifugal mechanism is removed, the initial amplified disturbance is apparently still able to maintain itself through the Reynolds shear-stress energy conversion mechanism from the mean flow, but is eventually and gradually overcome by the mechanism of viscous dissipation. We observe that in a flow visualization, if dye (in water) or smoke (in air) were trapped in the outer regions of a longitudinal vorticity system, such a system would appear to persist, and might possibly mask the deintensification (or intensification) within the outer boundaries, a possibility that emphasizes the role of detailed quantitative measurements. Nevertheless, the persistence of longitudinal vortices on a straight wall, following their initiation as initially amplified Görtler vortices, make the latter an attractive arrangement of forcing longitudinal vorticity elements in boundary layers (Yurchenko 1981 and personal communication, Kiev 1989).

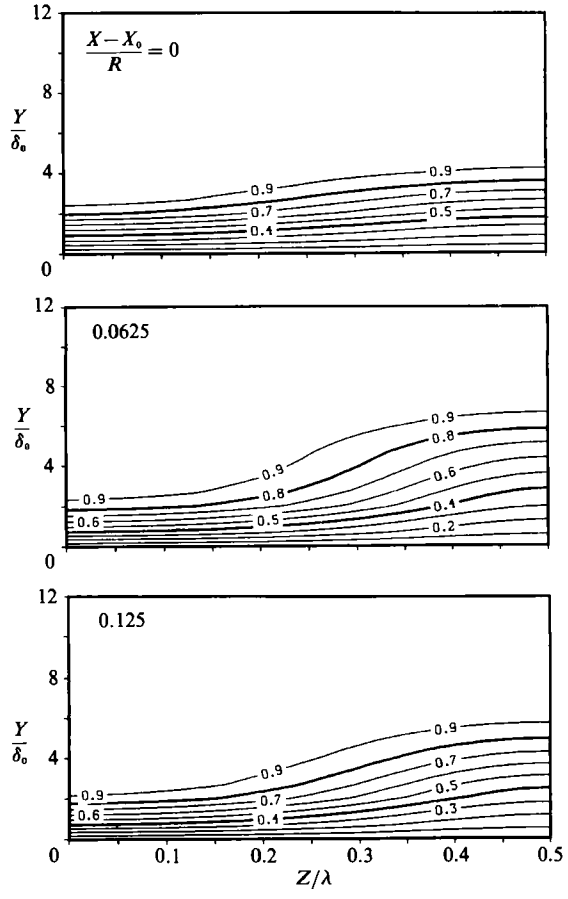

FIGURE 17. Developing of iso-U contours in the (y, z)-plane. Initiated Görtler vortices developing on straight wall. (Conditions correspond to Case 1, table 1.)

8.2. *Effect of decreasing the Görtler number*

In the previous section (Case 1), the Görtler number $G_\theta \sim R^{-\frac{1}{2}}$ was decreased to zero by attaching an 'infinite-radius', flat wall after the initiation of the Görtler vortices; correspondingly, $\Lambda_\lambda \sim R^{-\frac{3}{2}}$ also became zero. In the present Case 2 (see table 1) the initial Görtler number is decreased from 5.01 to the finite value of 2.51 and Λ_λ is decreased from 460 to 230 while keeping all other parameters fixed. Case 2 is still in the amplified region according to the linear parallel-flow theory (e.g. Floryan & Saric 1982). The development of constant-streamwise velocity contours in the cross-sectional plane is shown in figure 20. Although the stream-function contours are not shown here, their development is similar to but milder than in the standard case of §5.1. Thus the mildly amplified structure gives rise to incipient mushroom-like structures in the region computed in figure 20. The corresponding shear stress at the wall in the valley and peak regions are shown in figures 19(*a*) and 19(*b*). There is very little difference from the $G_\theta = 0$ case in the peak region, and only a slight difference is noted in the valley region. Both cases show a significant decrease in skin function compared to the standard case.

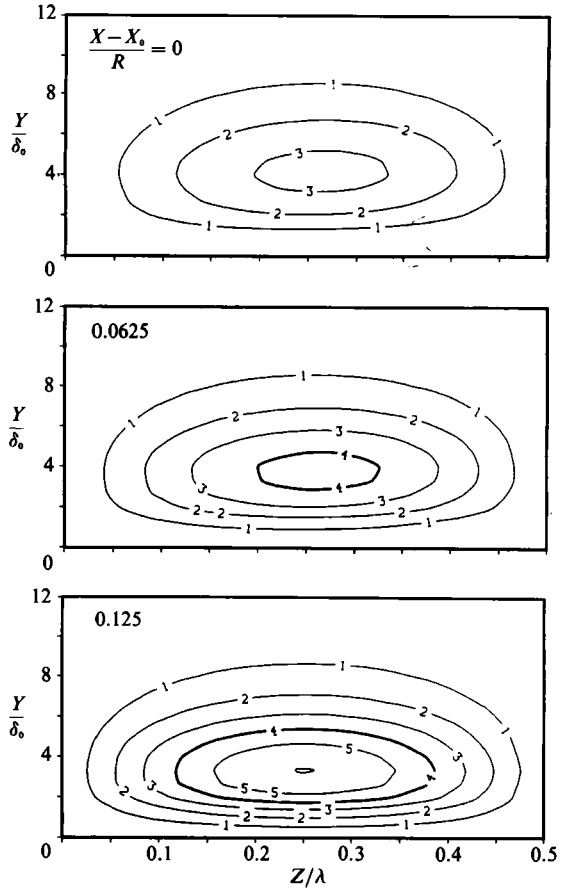

FIGURE 18. Stream-function development in the (y, z)-plane. (Conditions correspond to Case 1, table 1.)

8.3. *Effect of decreasing the initial disturbance amplitude*

In Case 3, the initial maximum linear Görtler vortex amplitude is decreased by a factor of four to $((u'^2/U_0^2)^{\frac{1}{2}}) \approx 0.03$ (see table 1). Because the other initial parameters are the same as in the standard case, the amplification is expected to be relatively more vigorous than the decreased Görtler-number cases of §§8.1 and 8.2. Because of the initial small amplitude, however, the curvature in the initial total streamwise velocity contour (figure 21) is barely noticeable, in contrast to that for the previous cases (figures 17, 20). However, because of the relatively larger G_θ and Λ_λ, the development (figure 21) is relatively more vigorous and, for the same $(X-X_0/R)$, the present case with lower initial amplitude but larger G_θ attains a similar nonlinear state (figure 21) as the case with relatively larger amplitude but smaller G_{θ_0} (figure 20). The ψ contours, not shown, exhibit amplification in $(X-X_0)/R$, expansion to the outer region of the boundary layer and migration of $\psi_{\max}$ towards the peak.

The valley- and peak-region shear-stress development is shown in figures 22 (*a*) and 22 (*b*). There is an appreciable reduction of shear stress in the valley region (figure 22*a*) due to the mild downwelling effect for the lower-initial-G_{θ_0} disturbance. Correspondingly, the weaker upwelling in the peak region is not sufficient to decrease

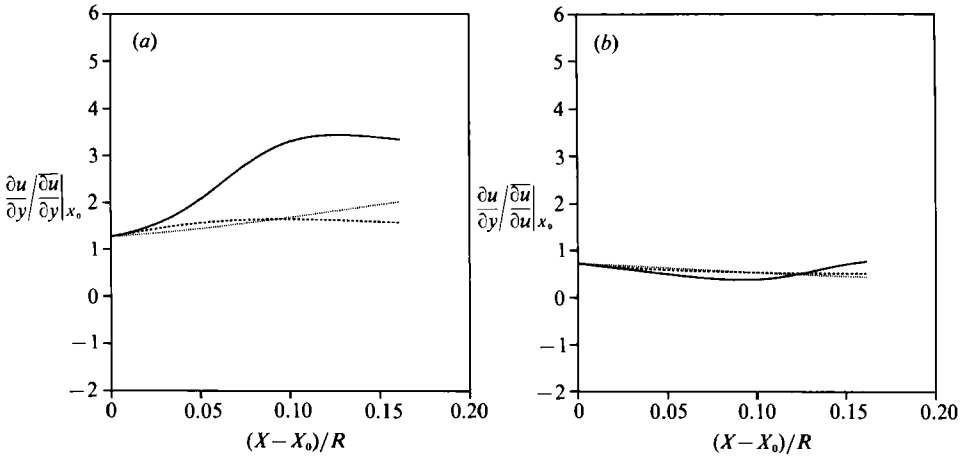

FIGURE 19. Streamwise velocity derivatives at the wall. (Conditions correspond to Cases 1 and 2, table 1.) ——, Standard case; – – –, Case 1; · · · · ·, Case 2. (*a*) At the valley, (*b*) at the peak.

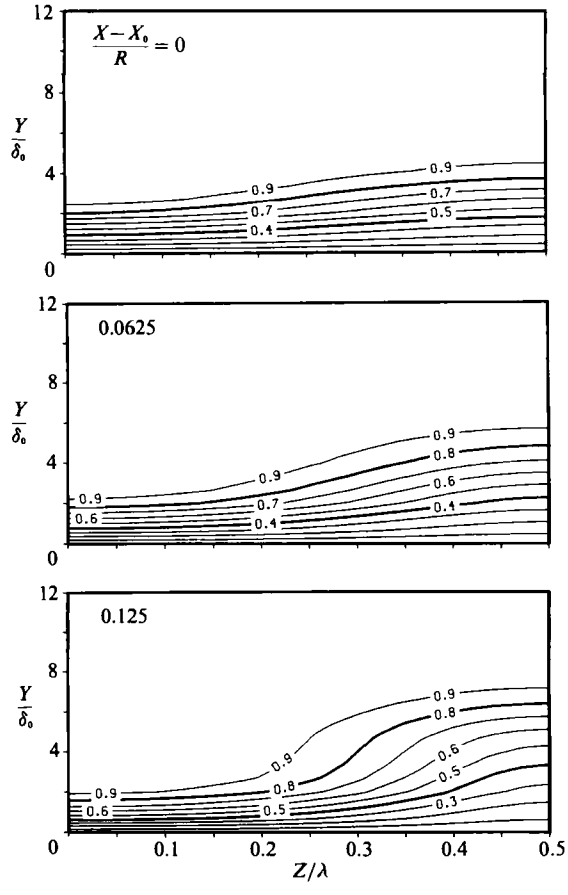

FIGURE 20. Development of iso-U contours in the (y,z)-plane: the effect of decreasing the initial Görtler number. (Conditions correspond to Case 3, table 1.)

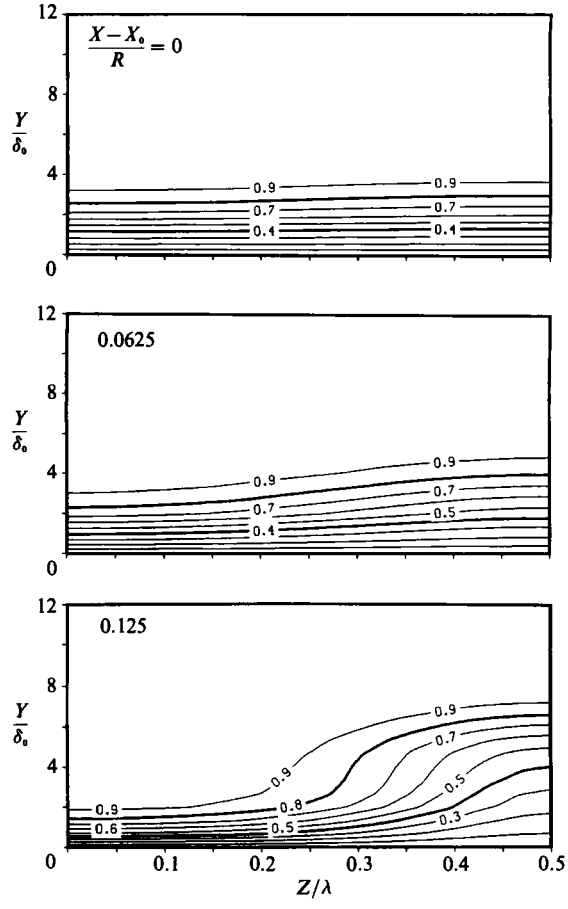

FIGURE 21. Development of iso-U contours in the (y,z)-plane: the effect of decreasing initial disturbance amplitude. (Conditions correspond to Case 3, table 1.)

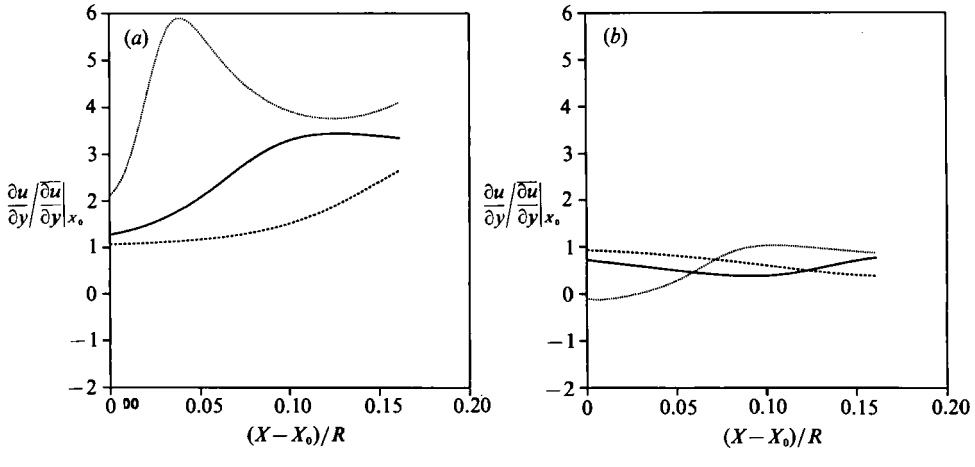

FIGURE 22. Streamwise velocity derivatives at the wall. (Conditions correspond to Cases 3 and 4, table 1.) ——, Standard case; · · · · ·, Case 3; – – – – –, Case 4. (*a*) At the valley, (*b*) at the peak.

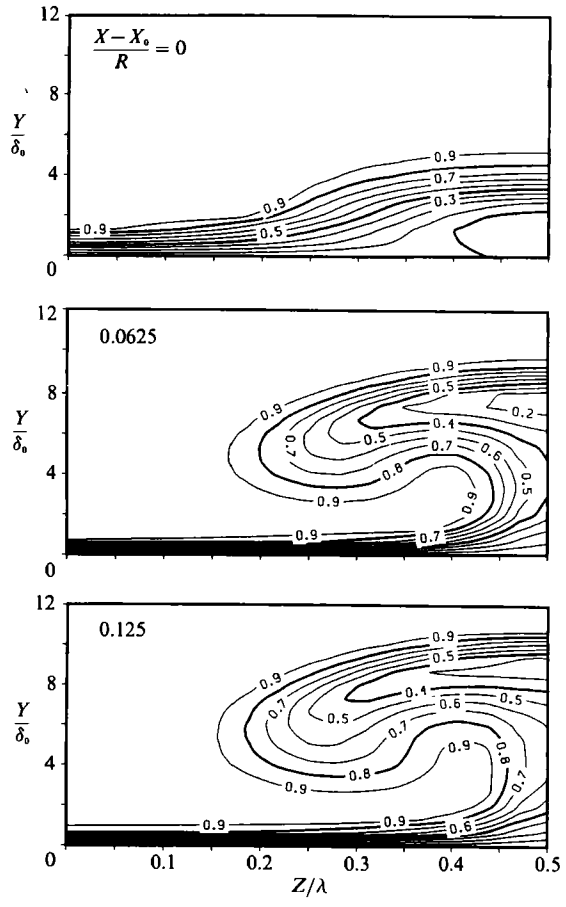

FIGURE 23. Development of iso-U contours in the (y,z)-plane: the effect of increasing initial disturbance amplitude. (Conditions correspond to Case 4, table 1.)

the streamwise momentum there, thus giving rise to a higher shear stress (figure 22*b*) in the major development region in $(X-X_0)/R$.

8.4. *Effect of increasing the initial disturbance amplitude*

In Case 4, the initial $[(\overline{u'^2})^{\frac{1}{2}}/U_0]_{\max}$ is increased to 0.48 (see table 1), a factor of four over the standard case and a factor of sixteen over Case 3. Because of the extreme increase in the initial amplitude, a small region of negative total-streamwise velocity appear in the peak region $\alpha z \approx \pi$ (figure 23) and is also manifested in the skin friction at the peak (figure 22*a*). However, this small negative region is very quickly obliterated in the nonlinear development. The vigorous initial amplitude leads to the much more rapid (relative to the standard case) development of mushroom-like structures in the constant-streamwise velocity contours (figure 23). The rapid development leads to an overshoot of the skin friction in the valley region (figure 22*a*), and also eventually in the peak region (figure 22*b*).

8.5. *Effect of decreasing the initial wavenumber*

In Case 5 the initial wavenumber is decreased by a factor of two from 0.308 to 0.154. Correspondingly, Λ_λ is increased from 460 to 1300 (see table 1). According to the

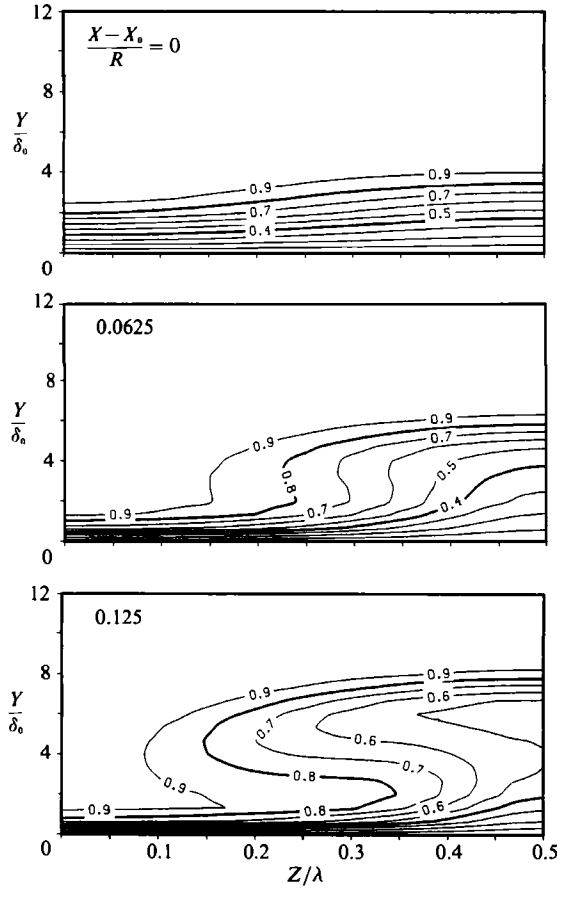

FIGURE 24. Development of iso-U contours in the (y,z)-plane: the effect of increasing initial Görtler wave number. (Conditions correspond to Case 5, table 1.)

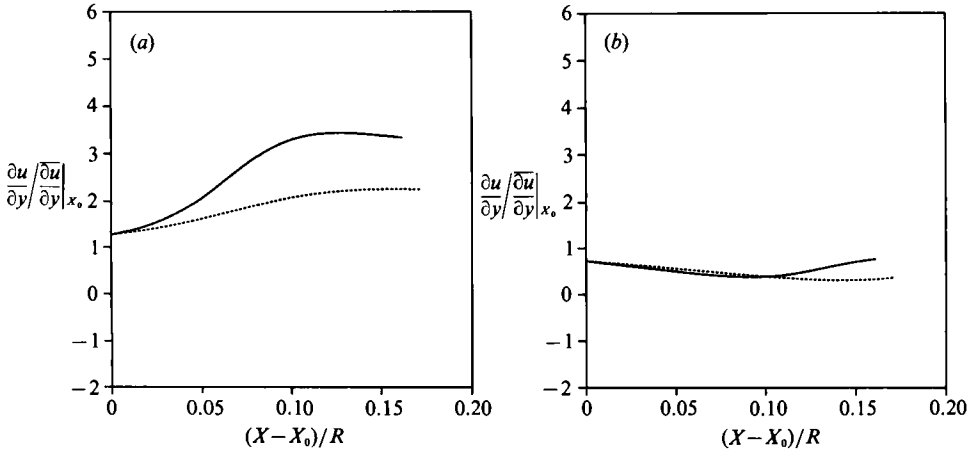

FIGURE 25. Streamwise velocity derivatives at the wall. (Conditions correspond to Case 5, table 1.) (*a*) At the valley, (*b*) at the peak.

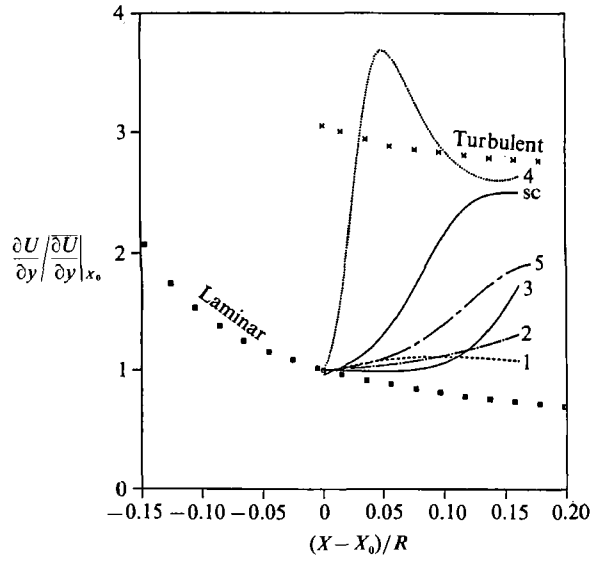

FIGURE 26. Development of spanwise averaged 'skin friction' $(\partial U/\partial Y)/(\partial U/\partial Y)_{X_0}$: the effect of parameter variations. (Conditions given in table 1: the numbers represent case numbers and SC refers to the standard case.)

linear parallel-flow theory (e.g. Floryan & Saric 1982), amplification rates for our initial disturbances (denoted by σ with a subscript corresponding to our case numbers and SC referring to the standard case) are such that $\sigma_{SC} (= \sigma_3 = \sigma_4) > \sigma_5 > \sigma_2 > \sigma_1$. Thus, for the same initial amplitude, the present Case 5 is expected to develop more vigorously at the outset than Cases 2 and 1. This is indeed the situation in terms of the constant-streamwise-velocity contours in figure 24: the vigorous development led to the development of mushroom-like contours similar to the intermediate stages of the standard case at $(X-X_0)/R = 100$. In terms of the effect on skin friction, figures 25(*a*) and 25(*b*) again show a significant decrease in the valley region, whereas there is little change up to $(X-X_0)/R \sim 0.10$ in the peak region.

8.6. *Skin friction*

The qualitative/quantitative effects of the initial parameters are best summarized in terms of the spanwise-averaged skin friction. Here it is normalized by its value at $(X-X_0)/R = 0$, and is shown in figure 26; the standard case and the laminar and turbulent skin friction are also shown for comparison. The standard value, equilibrating towards the turbulent skin friction, has already been compared with experiments (figure 6*b*).

The increase in initial amplitude, Case 3, the standard case and Case 4 in ascending magnitude, brings the transition process closer to $(X-X_0)/R = 0$. This is consistent with and expected from nonlinear analyses of developing free shear flows (e.g. Liu 1988*a*). The overshoot for large initial amplitude (Case 4) is quite spectacular. It is likely, however, that secondary instabilities would have developed earlier in this case than in SC, thus eroding the overshoot. Such secondary instabilities, resulting from initially strongly amplified Görtler vortices, still remain to be studied, although some progress has been reported (Sabry *et al.* 1989; Yu & Liu 1991).

The effect of decreasing the initial amplification rate (according to the linear, parallel-flow theory for the initial disturbances), is seen by comparing the standard

case and Cases 5 and 2 in decreasing order. Case 1 is special, and involves straightening the wall after initiation of the disturbance. The skin friction decreases in values as it develops in $(X-X_0)/R$ with decreasing initial disturbance amplification rates ($\sigma_2 < \sigma_5 < \sigma_{SC}$). Case 1 shows an eventual decrease in skin friction after an initial overshoot compared to Cases 2 and 5 (but not the standard case).

9. Further discussion: sites of secondary instabilities and transition to turbulence

The present contribution is intended to elucidate many facets of the nonlinear development of a longitudinal vorticity system in a laminar boundary layer undergoing transition. The initial disturbance with properties of linear Görtler vortices is used as a convenient and appropriate prototype for the study. Thus the dominant nonlinear stage in experimentally observed spatially developing situations is one of steady flow with a robust (once established) spanwise wavenumber. This observation made it possible to simplify the problem into a quasi-two-dimensional computation involving the cross-sectional plane, with time taking the place of the streamwise distance. The velocity components involved in the nonlinear development are, of course, fully three-dimensional.

The quantitative comparisons with the structural aspects of experiments in §5, which appear to be the first such comparisons for problems associated with Görtler vortices, lend considerable credibility to the use of computed results for the steady nonlinear development as the vehicle to study secondary instabilities and turbulence generation. Secondary instabilities of the nonlinearly evolved longitudinal vorticity system are reported elsewhere (Sabry *et al.* 1989; Yu & Liu 1991). The present work, however, addresses the sites of such secondary instabilities. The latter correspond, for instance, to the contours of the r.m.s. streamwise velocity associated with the time-dependent oscillations of predominantly 130 Hz frequency content in Swearingen & Blackwelder's (1987) measurements. The sites of such secondary instabilities are well correlated with sites of intense constant $\partial U/\partial Z$ contours in the cross-sectional plane. Similar contours are also obtained from the present computational results (§§5 and 7). In fact, the mechanism leading to the formation of intense $\partial U/\partial Z$ sites (on either side of the shoulders of the mushroom-like, nonlinearly developed, constant-U contours in the outer layer, and on either side of the base of the mushroom in the inner region) is believed to be the stretching and tilting mechanisms associated with the sources of the vertical vorticity η' and its enstrophy $\frac{1}{2}\overline{\eta'^2}$, as discussed in §7. It is, of course, obvious that the amplitude of the vorticity is just the r.m.s. of twice the enstrophy. Such quantities, and the balancing mechanisms leading to vorticity and enstrophy evolution, can be measured (Balint, Vukoslavcevik & Wallace 1988) with vorticity probes, and the probe size will be the limiting and filtering factor of the eddy sizes involved. The prospects of controlling flow development discussed in §8 through the control of initial parameters, and control of the sites of secondary instabilities and turbulence generation are a goal toward which continued studies would be most productive.

We acknowledge many beneficial conversations with J. T. Stuart. In particular, J. T. C. Liu has enjoyed two years of interaction with J. T. Stuart: 1987/88 in London and 1988/89 in Providence. Various aspects of this work were presented at the APS/DFD Annual Meetings (Sabry & Liu 1986, 1987, 1988*b*, 1989), The Symposium in Honour of C. C. Lin in 1987 at M.I.T. (Sabry & Liu 1988*a*), EUROMECH 228 at

University of Exeter (Liu 1987) and the 30th BTMC at Imperial College (Liu 1988*b*). This work is largely based on the first author's Ph.D thesis (Sabry 1988). It is partially supported by the National Science Foundation, Fluid, Particulate and Hydraulic Systems Program through NSF Grant MSM83-20307 monitored by Dr Stephen Traugott and by the Defense Advanced Research Projects Agency, Applied and Computational Mathematics Program through its University Research Initiative, monitored by Dr Helena S. Wisniewski; her strong support and enthusiasm were particularly appreciated. Partial support from the United Kingdom Science and Engineering Research Council through its Visiting Fellowship Programme, NATO Research Grant 343/85 and the National Science Foundation, US–China Cooperative Research Program, Grant INT85-14196 are acknowledged. We are very grateful to Xiuyang Yu for performing the additional computations discussed in §8. We are also grateful to Sandy Spinacci, Tina Trahan and Katrina Avery for the preparation of the manuscript.

REFERENCES

AIHARA, Y. & KOYAMA, H. 1981 Secondary instability of Görtler vortices. Formation of periodic three-dimensional coherent structure. *Trans. Japan Soc. Aero. Astron.* **24**, 78–94.

AIHARA, Y. & KOYAMA, H. 1982*a* Generation, development and distortion of longitudinal vortices in boundary layers along concave and flat plates. In *Three-dimensional Turbulent Boundary Layers* (ed. H. H. Fernholz & E. Krause), pp. 210–220. Springer.

AIHARA, Y. & KOYAMA, H. 1982*b* Nonlinear development and secondary instability of Görtler vortices. In *Stability in Mechanics of Continua* (ed. F. M. Schroeder), pp. 345–352. Springer.

AIHARA, Y., TOMITA, Y. & ITO, A. 1985 Generation, development and distortion of longitudinal vortices in boundary layers along concave and flat plates. In *IUTAM Symp. Novosibirsk 1984 on Laminar-Turbulent Transition* (ed. V. V. Kozlov), pp. 447–454. Springer.

AZIZ, K. & HELLUNS, C. 1967 A numerical study of the three-dimensional equations of motion for laminar natural convection. *Phys. Fluids* **10**, 314–324.

BABENKO, V. V. & YURCHENKO, N. F. 1980 Experimental investigation of Görtler instability on rigid and elastic flat plates. *Gidromekhanika* **41**, 103–108.

BALINT, J.-L., VUKOSLAVCEVIC, P. & WALLACE, J. M. 1988 The transport of enstrophy in a turbulent boundary layer. In *Proc. Zaric Memorial Intl Seminar on Wall Turbulence, Dubrovnik*.

BATCHELOR, G. K. 1967 *An Introduction to Fluid Dynamics*. Cambridge University Press.

BIPPES, H. 1972 Experimental study of the laminar-turbulent transition on a concave wall in a parallel flow. *NASA TM* 75243 (1978 translation).

BLACKWELDER, R. F. 1983 Analogies between transitional and turbulent boundary layers. *Phys. Fluids* **26**, 2807–2815.

BLACKWELDER, R. F. & KAPLAN, R. E. 1976 On the wall structure of the turbulent boundary layers. *J. Fluid Mech.* **76**, 89–112.

CLAUSER, M. & CLAUSER, F. 1937 The effect of curvature on transition from laminar to turbulent boundary layer. *NACA TN* 613.

CORINO, E. R. & BRODKEY, R. S. 1969 A visual investigation of the wall region in turbulent flow. *J. Fluid Mech.* **37**, 1–30.

DAGENHART, J. R. & MANGALAM, S. M. 1986 Disturbance functions of the Görtler instability on an airfoil. *AIAA Paper* 86-1048.

DAVEY, A., DIPRIMA, R. C. & STUART, J. T. 1968 On the instability of Taylor vortices. *J. Fluid Mech.* **31**, 17–52.

FLORYAN, J. M. & SARIC, W. S. 1982 Stability of Görtler vortices in boundary layers. *AIAA J.* **20**, 316–324.

FRAZER, R. A. 1931 Stability of unsteady rotary fluid motions within an infinite circular cylinder. *Aeron. Res. Comm. Rep.* T.3112 (F.M. 42).

GÖRTLER, H. 1940 On the three-dimensional instability of laminar boundary layers on Concave Walls. *Nachr. Ges. Wiss. Göttingen* **2**, 1–26 (*NACA TM* 1375, 1954).

GRASS, A. J. 1971 Structural features of turbulent flow over smooth and rough boundaries. *J. Fluid Mech.* **50**, 233–255.

GUEZENNEC, Y. G., PIOMELLI, U. & KIM, J. 1989 Structures in turbulent channel flow. *Phys. Fluids* A **1**, 764–766.

HALL, P. 1982*a* Taylor–Görtler vortices in fully developed or boundary layer flows: linear theory. *J. Fluid Mech.* **124**, 475–494.

HALL, P. 1982*b* On the nonlinear evolution of Görtler vortices in nonparallel boundary layers. *IMA J. Appl. Maths* **29**, 173–196.

HALL, P. 1983 The linear development of Görtler vortices in growing boundary layers. *J. Fluid Mech.* **130**, 41–58.

HALL, P. 1988 The nonlinear development of Görtler vortices in growing boundary layers. *J. Fluid Mech.* **193**, 243–266.

HALL, P. 1989 Görtler vortices in growing boundary layers: The leading edge receptivity problem, linear growth and the nonlinear breakdown stage. *ICASE Rep.* 89-81.

HALL, P. & LAKIN, W. 1988*a* The fully nonlinear development of Görtler vortices in growing boundary layers. *Proc. R. Soc. Lond.* A **415**, 421–444.

HALL, P. & LAKIN, W. 1988*b* Instability driven boundary layers on curved walls. In *Symp. Honor C. C. Lin* (ed. D. J. Benney, F. H. Shu & C. Yuan), pp. 134–143. World Scientific.

HALL, P. & SEDDOUGUI, S. 1989 On the onset of three-dimensionality and time-dependence in Görtler vortices. *J. Fluid Mech.* **204**, 405–420.

HAMA, R. R. & NUTAANT, J. 1963 Detailed flow-field observations in the transition process in a thick boundary layer. In *Proc. 1963 Heat Trans. Fluid Mech. Inst.*, pp. 77–93. Palo Alto: Stanford University Press.

HAMMERLIN, G. 1955 Uber das Eigenwertproblem der dreidimensipnalen Instabilitat laminarer Grenzschichten an konkaven Wanden. *J. Rat. Mech. Anal.* **4**, 279–321.

HERBERT, T. 1976 On the stability of the boundary layer along a concave wall. *Archiwum Mechaniki Stosowane* (Warszawa) **28**, 1039–1055.

HERBERT, T. 1987 Secondary instability of boundary layers. *Ann. Rev. Fluid Mech.* **20**, 487–526.

ITO, A. 1980 The generation and breakdown of longitudinal vortices along a concave wall. *J. Japan Soc. Aerospace Sci.* **28**, 327–333.

ITO, A. 1985 Breakdown structure of longitudinal vortices along a concave wall. *J. Japan Soc. Aerospace Sci.* **33**, 166–173.

JONES, C. A. 1981 Nonlinear Taylor vortices and their stability. *J. Fluid Mech.* **102**, 249–261.

JONES, C. A. 1985 The transition to wavy Taylor vortices. *J. Fluid Mech.* **157**, 135–162.

KIM, J., KLINE, S. & REYNOLDS, W. C. 1971 The production of turbulence near a smooth wall in a turbulent boundary layer. *J. Fluid Mech.* **50**, 133–160.

KLEBANOFF, P. S., TIDSTROM, K. D. & SARGENT, L. M. 1962 The three-dimensional nature of boundary-layer instability. *J. Fluid Mech.* **12**, 1–34.

KLINE, S. J., REYNOLDS, W. C., SCHROUT, F. A. & RUNSTAEDLER, P. W. 1967 The structure of turbulent boundary layers. *J. Fluid Mech.* **30**, 741–773.

KOVASZNAY, L. S. G., KOMODA, H. & VASUDERA, B. R. 1962 Detailed flow field in transition. In *Proc. 1962 Heat Trans. Fluid Mech. Inst.*, pp. 1–26. Palo Alto: Stanford University Press.

KOZLOV, L. F., CIGANUK, A. I., BABENKO, V. V., NIKISHOVA, O. D. & VOROPAYEV, G. A. 1985 *Formation of Turbulence in Shear Flows*, pp. 180–215. Kiev: Naukova Dumka (in Russian).

KOZLOV, L. F., GLUSHKO, V. N. & NIKISHOVA, O. D. 1981 Experimental study of the generation of Görtler vortices in an unsteady boundary layer. *Fluid Mech.-Sov. Res.* **10**, 89–95. (Originally appeared in *Gidromekhanika* **45**, 61–65, 1982).

LIEPMANN, H. W. 1943 Investigation on laminar boundary-layer stability and transition on curved boundaries. *NACA Wartime Rep.* W-107.

LIEPMANN, H. W. 1945 Investigation of boundary layer transition on concave walls. *NACA Wartime Rep.* W-87.

LIU, D. C. S. & CHEN, C. F. 1973 Numerical experiments on time-dependent rotational Couette flow. *J. Fluid Mech.* **59**, 77–95.

LIU, J. T. C. 1971 Nonlinear development of an instability wave in a turbulent wake. *Phys. Fluids* **14**, 2251–2257.

LIU, J. T. C. 1974 Developing large-scale wavelike eddies and the near jet noise field. *J. Fluid Mech.* **62**, 437–543.

LIU, J. T. C. 1987 The generation of high intense shear layers by the nonlinear development of Görtler vortices. *EUROMECH 228: Boundary Layer Instability and Transition, September 21–25, University of Exeter.*

LIU, J. T. C. 1988*a* Contributions to the understanding of large-scale coherent structures in developing free turbulent shear plane. *Adv. Appl. Mech.* **26**, 183–309.

LIU, J. T. C. 1988*b* Longitudinal vorticity elements in boundary layers. *Keynote Lecture, 30th British Theoretical Mechanics Colloquium, April 11–15, Imperial College, London.*

LIU, J. T. C. & KAPTANOGLU, H. T. 1987 Control of free shear layers. *AIAA Paper* 87-2689.

LIU, J. T. C. & KAPTANOGLU, H. T. 1989 Multiple large-scale coherent structures in free turbulent shear flows. In *IUTAM Second European Turbulence Conf.* (ed. H. A. Fernholz & H. E. Fiedler). Springer.

MANGALAM, S. M., DAGENHART, J. R., HEPNER, T. F. & MEYERS, J. F. 1985 Görtler instability on a airfoil. *AIAA Paper* 85-0491.

MEKSYN, D. & STUART, J. T. 1951 Stability of viscous motion between parallel planes for finite disturbances. *Proc. R. Soc. Lond.* A **208**, 517–526.

MOORE, D. W. 1985 The interaction of a diffusing line vortex and an aligned shear flow. *Proc. R. Soc. Lond.* A **399**, 367–375.

NIKITOPOULOS, D. E. & LIU, J. T. C. 1990 *Second IUTAM Symp. Structure of Turbulence and Drag Reduction* (ed. A. Gyr). Springer.

PEACEMAN, D. W. & RACHFORD, H. H., JR 1955 The numerical solution of parabolic and elliptic differential equations. *SIAM J. Appl. Maths* **3**, 28–41.

PEARSON, C. E. 1965 A computational method for viscous flow problems. *J. Fluid Mech.* **21**, 611–622.

PEARSON, C. F. K. & ABERNATHY, F. H. 1984 Evolution of the flow field associated with a streamwise diffusing vortex. *J. Fluid Mech.* **146**, 271–283.

PEERHOSSAINI, H. 1984 On the subject of Görtler vortex. In *Cellular Structures in Instabilities* (ed. J. E. Wesfreid & S. Zaleski), pp. 376–384. Springer.

PEERHOSSAINI, H. 1985 Les Tourbillons de Görtler. *Lab. d'Hydrodynamique et Mec. Phys., ESPCI Rep.* R-86-24.

PEERHOSSAINI, H. & WESFREID, J. E. 1988 On the inner structure of streamwise Görtler roles. *Intl J. Heat Fluid Flow* **9**, 12–18.

PETITJEANS, P., PEERHOSSAINI, H. & WESFREID, J. E. 1990 Nonlinear investigation of the Taylor–Görtler vortices. Abstract in *Coll. Görtler Vortex Flow, Euromech 271.*

PRANDTL, L. 1935 *Aerodynamic Theory 3*, p. 34. Springer.

RUSSELL, J. M. & LANDAHL, M. T. 1984 The evolution of a flay eddy near a wall in an inviscid shear flow. *Phys. Fluids* **27**, 557–570.

SABRY, A. S. 1988 Numerical computation of the nonlinear evolution of Görtler vortices. Ph.D. thesis, Brown University, Division of Engineering.

SABRY, A. S. & LIU, J. T. C. 1986 Nonlinear Görtler vortices and energy transfer between spanwise modes. *Bull. Am. Phys. Soc.* **30**, 1696.

SABRY, A. S. & LIU, J. T. C. 1987 On the generation of high intense shear layers from nonlinear development of Görtler vortices. *Bull. Am. Phys. Soc.* **32**, 2096.

SABRY, A. S. & LIU, J. T. C. 1988*a* Nonlinear development of Görtler vortices and the generation of high shear layers in the boundary layer. In *Symp. to Honor C. C. Lin* (ed. D. J. Benney, F. H. Shu & C. Yuan), pp. 175–186. World Scientific.

SABRY, A. S. & LIU, J. T. C. 1988*b* On the nonlinear development of vorticity and enstrophy during the transition over slightly curved surfaces. *Bull. Am. Phys. Soc.* **33**, 2260.

SABRY, A. S. & LIU, J. T. C. 1989 On the secondary instability in the transition process in wall bounded shear flows. *Bull. Am. Phys. Soc.* **34**, 2268.

SABRY, A. S., YU, X. & LIU, J. T. C. 1989 Secondary instabilities of three-dimensional inflectional velocity profiles resulting from longitudinal vorticity elements in boundary layers. In *Proc. IUTAM 3rd Symp. on Laminar-Turbulent Transition* (ed. R. Michel & D. Arnal). Springer.

SARIC, W. S. 1992 Görtler vortices. *Ann. Rev. Fluid Mech.* **24**, (to appear).

SCOTT, M. R. & WATTS, H. A. 1977 Computational solutions of linear two-point boundary values via orthonormalization. *SIAM J. Numer. Anal.* **14**, 40–70.

SHIGEMI, M., JOHNSON, M. W. & GIBBINGS, J. C. 1987 Boundary layer transition on a concave surface. *IMechE Paper* C262/87.

SMITH, A. M. O. 1955 On the growth of Taylor–Görtler vortices along highly concave walls. *Q. Appl. Maths* **13**, 233–262.

STUART, J. T. 1965 The production of intense shear layers by vortex stretching and convection. *NPL Aero. Res. Rep.* 1147; also *NATO AGARD Rep.* 514.

STUART, J. T. 1986 Instability of flows and their transition to turbulence (*24th L. Prandtl Memorial Lecture, Dortmund*). *Z. Flugwiss. Weltraumforsch.* **10**, 379–392.

STUART, J. T. 1987 Instability, three-dimensional effects and transition in shear flows. In *Perspectives in Turbulence* (ed. P. Bradshaw & H. U. Meier), pp. 1–25. Springer.

STUART, J. T. 1988 Nonlinear Euler partial differential equations: singularities in their solution. In *Symp. to Honor C. C. Lin* (ed. D. J. Benney, F. H. Shu and C. Yuan), pp. 175–186. World Scientific.

SWEARINGEN, J. D. & BLACKWELDER, R. F. 1987 The growth and breakdown of streamwise vortices in the presence of a wall. *J. Fluid Mech.* **182**, 255–290.

TANI, I. 1962 Production of longitudinal vortices in the boundary layer along a curved wall. *J. Geophys. Res.* **67**, 3075–3080.

TANI, I. & AIHARA, Y. 1969 Görtler vortices and boundary layer transition. *Z. Angew. Math. Phys.* **20**, 609–618.

TANI, I. & KOMODA, H. 1962 Boundary layer transition in the presence of streamwise vortices. *J. Aerospace Sci.* **29**, 440–444.

TAYLOR, G. I. 1923 Stability of a viscous liquid contained between two rotating cylinders. *Phil. Trans. R. Soc. Lond.* A **223**, 289–343.

TENNEKES, J. & LUMLEY, J. L. 1972 *A First Course in Turbulence.* MIT Press.

THOMPSON, J. F., WARSI, Z. U. A. & MASTIN, C. W. 1985 *Numerical Grid Generation.* North Holland.

WILLMARTH, W. W. 1975 Structure of turbulence in boundary layers. *Adv. Appl. Mech.* **15**, 159–254.

WINOTO, S. H. & CRANE, R. I. 1980 Vortex structure in laminar boundary layers on a concave wall. *Intl J. Heat Fluid Flow* **2**, 221–231.

WORTMANN, F. X. 1969 Visualization of transition. *J. Fluid Mech.* **38**, 473–480.

YANG, Z. 1987 A single streamwise vortical structure and its instability in shear flows. Ph.D. thesis, Harvard University.

YU, X. & LIU, J. T. C. 1991 The secondary instability in Görtler flow. *Phys. Fluids* A **3** (to appear).

YURCHENKO, N. F. 1981 Method of experimental investigation of a system of longitudinal vortices in the boundary layer. *Inzhenerno-Fiz. Zh.* **41**, 996–1002.

YURCHENKO, N. F., BABENKO, V. V. & KOZLOV, L. F. 1979 Experimental investigation of Görtler instability in the boundary layer. In *Stratified and Turbulent Flows*, pp. 50–59. Kiev: Naukova Dumka (In Russian).